ISSN 0016-7029, Geochemistry International, 2025, Vol. 63, No. 5, pp. 361–390. © Pleiades Publishing, Ltd., 2025.

Timing and Sequence of Endogenous Events in the Bug Granulite–Gneiss Domain of the Ukrainian Shield Based on the Study of a Composite Tectono-Magmatic Breccia

S. B. Lobach-Zhuchenko[a, †], **Sh. K. Baltybaev**[a, b, *],
Yu. S. Egorova[a], **A. V. Yurchenko**[a], and **O. L. Galankina**[a]

[a] *Institute of Precambrian Geology and Geochronology, Russian Academy of Sciences, St Petersburg, 199034 Russia*
[b] *St. Petersburg State University, Earth's Science Institute, St. Petersburg, 199034 Russia*
**e-mail: shauket@mail.ru*

Received January 9, 2025; revised January 9, 2025; accepted February 17, 2025

Abstract—In the Bug granulite-gneiss domain of the Ukrainian shield, a composite tectono-magmatic breccia including enderbites and various mafic rocks was studied in the gneiss-enderbite complex. Based on the assessment of the thermodynamic conditions of rock and mineral formation and the analysis of the U–Pb and Lu–Hf isotope systems of zircon, the endogenous history of the gneiss–enderbite complex is deciphered. The predominant rocks are enderbites with numerous enclaves of two-pyroxene and pyroxene–amphibole crystalline schists that were deformed under granulite facies metamorphism. The oldest zircons have a concordant U-Pb age of 3.6–3.7 Ga, which is close to the age of the protolith of the Bug enderbites. The zircons are characterized by a heterogeneous structure, negative εHf(t) values from –1 to –38, and a variation in ^{176}Hf/^{177}Hf$_{(0)}$ isotope ratios from 0.28035 to 0.28095, which is consistent with their different ages and origins. Based on the age, geochemistry, and isotope composition of zircon from composite breccia rocks, following geological events from Archean to Proterozoic are distinguished: (1) 3.67–3.60 Ga stage of magmatic crystallization of early mineral associations; (2) 3.0–2.8 Ga stage of granulite metamorphism and partial melting (2.9 Ga) of the enderbites with the preservation of melt mineral phases in zircons, but with a strong disturbance of its U-Pb isotope system; (3) 2.0–1.9 Ga stage of Proterozoic granulite metamorphism with the reorganization of cation and isotope systems of rock-forming and accessory minerals. The obtained data are consistent with the model of polychronous evolution of the continental crust of the Ukrainian Shield in the Paleo- and Mesoarchean with its strong reworking in the Paleoproterozoic.

Keywords: Zircon, geochemistry, age, metamorphism, tectono-magmatic breccia, Ukrainian shield, enderbite

DOI: 10.1134/S0016702925600026

INTRODUCTION

Granulite–gneiss and granite–greenstone domains are the main Archean tectonic structures and their study is of great importance for reconstructing the early Earth's history. However, due to the repeated tectonometamorphic reworking, the granulite–gneiss domains are much poorer preserved than the granite–greenstone domains. As was demonstrated by the example of the granite–gneiss domains of Antarctica, Northern Labrador, and other regions (Hartlaub et al., 2006), the oldest rocks of these structures are orthogneisses with ages of 3.7–3.9 Ga (Saglek complex, Labrador, Schiotte et al., 1989) and 3.84–3.97 Ga (Napier complex, Antarctica, Harley and Black, 1997). At the same time, the orthogneisses of the granite–greenstone domains, for instance, Acasta gneisses in the Slave craton have an older age of 4.03 Ga (Stern and Bleeker, 1998), in spite of the fact that the rocks were subjected to the multiple superimposed magmatic and metamorphic transformations up to the Proterozoic 1800–1700 Ma (Reimink et al., 2016).

Similar and frequently ambiguous ages of Precambrian rocks complicate the correlation of geological events even within a single geological province. For instance, this is the case for the Bug granulite–gneiss domain (BGGD) of the Ukrainian shield. The domain consists of volcanosedimentary and magmatic complexes formed within over 2 Ga (Bibikova et al., 2013; Claesson et al., 2015; Lobach-Zhuchenko et al., 2013, 2017). U-Pb age of the oldest zircon cores from the BGGD ortogneisses is 3.75–3.80 Ga (Bibikova et al., 2013; Lobach-Zhuchenko et al., 2013; Lobach-Zhuchenko et al., 2013, 2017; 2022; 2023; Claesson et al., 2019), while the oldest dated metavolcanic rocks have an U-Pb age of 3628 ± 38 Ma (Lobach-Zhuchenko et al., 2017). These rocks were overprinted

---

[†] Deceased.

by later processes of 2.75–2.85 and 2.0–1.8 Ga (Bibikova et al., 2013; Claesson et al., 2015; Lobach-Zhuchenko et al., 2017).

The aforementioned endogenous events were revealed in spatially separated geological objects, which significantly complicated their correlation. In this relation, it was necessary to find the key objects in BGGD, which could preserve the most complete record of endogenous events with distinct structural and compositional relations of rocks within exposures. The study of such rocks offers an opportunity to obtain a highly reliable scale of tectonometamorphic and magmatic events in the region and to avoid errors related to the possible inaccurate correlations of episodes of endogenous activity based on the spatially separated geological objects.

In recent years, we have studied the gneiss-enderbite complex including a large tectonized lens (below termed as tectonometamorphic breccia) within BGGD. The results of these studies are discussed in this work. The sequential evolution of the gneiss-enderbite complex can be deciphered by studying the rocks and minerals, the assessment of thermodynamic conditions of formation, and analysis of U–Pb and Lu–Hf zircon systems of enderbites and diverse mafic rocks that form a composite tectonomagmatic breccia. To this aim, the methods of analysis of isotope zircon systems and estimation of *PT*-conditions of rock formation were applied to reconstruct the time scale of the Precambrian geological events in the studied region.

ANALYTICAL

The content of major elements in the rocks was determined by conventional chemical technique at the Analytical Laboratory of the Geological Institute of the Federal Science Center of RAS (Apatity), while trace elements were determined at the Laboratory of the Analytical Center of the Karelian Research Centre (Petrozavodsk); the technique and accuracy of measurements were considered in the work (Svetov et al., 2015).

The mineral composition was studied using a JEOL JSM-6510LA scanning electron microscope equipped with a JEOL JED-2200 EDS at the Institute of Precambrian Geology and Geochronology of the Russian Academy of Sciences (IPGG RAS, St. Petersburg); the measurement technique was reported in (Lobach-Zhuchenko et al., 2022).

U–Th–Pb isotope studies and U and Pb isotope analysis were performed on a SHRIMP-II secondary ion microprobe at the Center of Isotopic Research of the Karpinsky Institute (St. Petersburg). Data points for isotope analysis were preliminarily selected using CL (cathodoluminescence) and BSE (back-scattered electrons) zircon images. Analytical data were processed according to (Williams, 1998) using softwares Squid-1.13a (Ludwig, 2005) and Isoplot-3.75 (Ludwig, 2012). The method of determination of concentrations of trace elements and isotope analysis of zircons are given in more detail in (Lobach-Zhuchenko et al., 2017).

The Lu and Hf isotope composition of zircon was determined by LA-ICP-MS using a DUV-193 (New Wave Research) laser ablation system with 193 nm Ar-F eximer COMPex-102 (Lambda Physik) laser coupled to a Thermo Finnigan Neptune multichannel mass-spectrometer at the Center of Isotopic Research of the Karpinsky Institute, St. Petersburg. All ratios were corrected for mass discrimination by normalizing to the ^{178}Hf/^{177}Hf ratio. The isobaric interferences of ^{176}Yb and ^{176}Lu on ^{176}Hf value were corrected by measuring the interference-free ^{172}Yb and ^{175}Lu. The applied technique was described in works (Griffin et al., 2000; 2012). The laser beam diameter during zircon analysis was ~50–70 μm. The measurements were controlled using standard set of GJ-1, MudTank, and Temora in the diagram. Typical measurement errors were no more than 0.015% for ^{176}Hf/^{177}Hf and around 0.5% for ^{176}Lu/^{177}Hf, the measurement error of $\varepsilon_{\mathrm{Hf}}$(t) is ±1.5. The $\varepsilon_{\mathrm{Hf}}$(t) values and initial (^{176}Hf/^{177}Hf)$_i$ ratios were calculated using the following CHUR(0) parameters: ^{176}Hf/^{177}Hf = 0.282785, ^{176}Lu/^{177}Hf = 0.0336 (Bouvier et al., 2008) and decay constants ^{176}Lu = 1.865 × 10^{-11} yr^{-1} (Scherer et al., 2001); two-stage Lu–Hf isotope model age was calculated using DM model according to (Griffin et al., 2000).

The pressure of mineral formation was estimated using mineral compositions and geobarometers Opx–Cpx[1] (Putirka, 2008), Amp–Pl (Molina et al., 2015), Amp (Hammarstrom et al., 1986; Hollister et al., 1987; Johnson, Rutherford, 1989; Schmidt, 1992).

Crystallization temperature of zircon and biotite was calculated using Ti content according to (Watson et al., 2006; Ferry and Watson, 2007) and (Henry et al., 2005), respectively.

The crystallization temperature of Opx in association with Cpx was estimated using two-pyroxene (Wood and Banno, 1973; Wells, 1977; Taylor, 1998; Putirka, 2008; Witt-Eickschen and O`Neil, 2005) or single-pyroxene thermometers (Mercier, 1980; Simakov, 2008). The Amp–Pl equilibrium temperature was calculated using thermometer (Holland and Blundy, 1994).

GEOLOGICAL POSITION AND STRUCTURE OF THE COMPOSITE BRECCIA

The Bug granulite–gneiss domain is located in the south of the Dniester–Bug province, where the oldest rocks were recovered in the Odessky, Kazachii Yar, and Gaivaronsky quarries (Figs. 1a, 1b). This domain was distinguished based on the lowered rock density in the gravity anomaly map and a weak anomaly related

---

[1] Abbreviation was given after (Whitney and Evans, 2010).

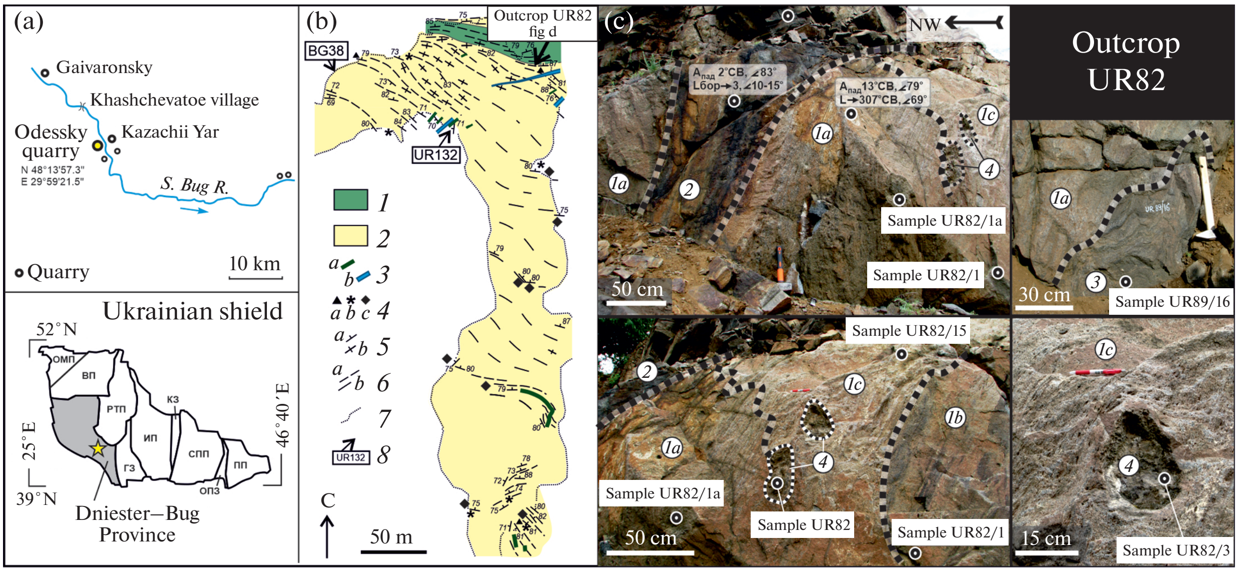

Fig. 1. Location of the Odessky quarry in the topographic scheme (a) and in the scheme of the Ukrainian shield (b), geological scheme and outlines of the quarry with indication of main types of the studied rocks (c) and their relations within outcrops (d). Inset (b) shows: a scheme of tectonic structure of the Ukrainian shield with indication of the studied area (shown by asterisks): provinces: (IP) Ingul, (VP) Volhyn Province, (AP) Azov Province, (RTP) Ros-Tikich Province, (MDP) Middle Dnieper Province; suture zones: (GZ) Golovanensk, (KZ) Krivoy Rog, (OPZ) Orekhovo-Pavlograd; (OMB) Osnitsk–Mikashevichi Belt. Symbols (c): (*1*) crystalline schists (metavolcanic rocks), quartzites, garnet, garnet–pyroxene, and garnet–magnetite quartzites; (*2*) gneiss enderbites; (*3*) dikes: (a) metagabro, (b) trachybasalts; (*4*) mafic inclusions: (a) metaorthopyroxenites, (b) metaperidotites, (c) crystalline schists (mafic rocks); (*5*) foliation and banding in zones of sublatitudinal shearing ((a) inclined, (b) vertical); (*6*) early NW-trending shearing and banding ((a) inclined, (b) vertical); (*7*) contour of the quarry; (*8*) sample localities and numbers. Circled numbers in Fig. (d): (*1*) gneiss enderbites: (a) leucocratic, (b) mesocratic, (c) domain of leucosome development; (*2*) lens of crystalline schists; (*3*, *4*) mafic inclusions: (*3*) fine-grained crystalline schists, (*4*) metaorthopyroxenites.

to the development of moderate- to low-Mg rocks in the total magnetic field map (Kislyuk et al., 2011).

The studied breccia (exposure UR82) is located in in the northeastern wall of the Odessky quarry (48°13′57.3″ N, 29°59′21.5″ E) (Fig. 1c). It is made up mainly of gneiss-enderbites with numerous enclaves of pyroxene and pyroxene–amphibole crystalline schists, garnet, garnet–magnetite quartzites, and other metamafic rocks.

The aforementioned rocks experienced three stages of deformations: (1) NW-trending deformation D_{n+1}, (2) sublatitudinal shears D_{n+2}, 3) local zones of NE-trending deformations D_{n+3}, which were accompanied by the emplacement of metabasaltic and trachybasaltic dikes. All the deformations occurred under the granulite facies conditions with a slight pressure decrease to the stage D_{n+3} (Lobach-Zhuchenko et al., 2017).

The composite breccia is confined to the D_{n+2} shear deformation zone, near the tectonic contact between gneiss enderbites and crystalline schists (Fig. 1c). The contact plane of these rocks at a small angle cuts across shearing and banding of the crystalline schists. The latter retain signs of repeated deformations: relict of limbs of NW-trending compressed folds dipping at 75–85° to NE as well as relicts of open folds with horizontal orientation of axial planes in the northern part. To the south, the strike of the plane structures of the crystalline schists changes into latitudinal one: NW 275° at NE dip at 75–80°. The latest deformations (NW → 2°∠83°) are characterized by a low-angle lineation (L → 3 ∠10–158) and are accompanied by the growth of amphibole and garnet.

Enderbites that are in direct contact with crystalline schists are exposed in sublatitudinal direction for 10–11 m, and represent a tectonic breccia in a sublatitudinal shear zone. The visible width of the gneiss enderbite exposures is 1.2 m. The orientation of gneissosity and banding of enderbites is NW 283° → NE ∠79°, L → NW 307° ∠69°. Low-angle lineation similar to the late lineation in the crystalline schists is locally observed.

Mafic enclaves are represented by numerous small and one larger fragment (Fig. 1d) of fine-grained crystalline schists and small round enclaves of metaorthopyroxenites. The thickness of the breccia zone decreases southward with transition to enderbites with preserved early gneissosity.

Breccia cement consists of compositionally and structurally heterogeneous enderbites (Fig. 1d). The latter are locally migmatized with the appearance of leucosomes consisting of quartz–plagioclase material and several mafic minerals.

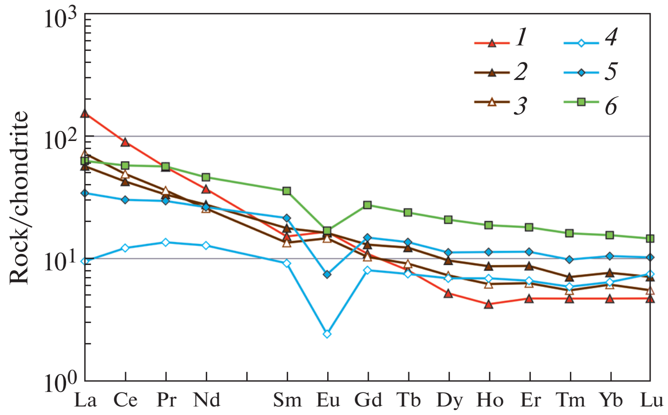

Fig. 2. Chondrite-normalized (Sun and McDonough, 1989) REE distribution in the rocks of tectonomagmatic breccia. (*1*) leucocratic enderbite UR82/1a; (*2*) mesocratic enderbite UR82/1; (*3*) leucosome UR82/15; (*4*) metapyroxenite UR82; (*5*) metapyroxenite UR82/3; (*6*) amphibole–pyroxene schist UR89/16.

CHARACTERISTICS OF ROCKS AND COMPOSITIONS OF ROCK-FORMING MINERALS

The results of chemical analysis of rocks and minerals are listed in Table EMS1 in Supplementary.

The matrix of the tectonomagmatic breccia is made up of leucocratic or mesocratic enderbites having heterogeneous mineral composition and structure (Fig. 1d), and locally containing leucosome.

Leucocratic enderbite (sample UR82/1a) has massive granoblastic texture, consists of plagioclase, K-feldspar, quartz, biotite, two pyroxenes, magnetite, as well as accessory apatite and zircon. Chemically, it corresponds to tonalite, and in terms of REE content and fractionation $(La/Yb)_n = 33$ resembles Archean tonalite (Moyen and Martin, 2012), but differs in the higher mafic index and #mg, and five times higher concentrations of siderophile elements (Ni + Cr). In the diagram SiO_2 vs FeO/(FeO + MgO) (Frost et al., 2001), it is ascribed to the magnesian granitoids and close to the mantle derivatives (Hui et al., 2011). The rocks show the absence of Eu anomaly, flat HREE pattern, at higher LREE (Fig. 2, Table 1).

Mesocratic enderbite (sample UR 82/1) is restricted to the highly sheared part of the exposure, and has a banded structure caused by the alternation of melanocratic and leucocratic minerals. The rock contains early mineral assemblage: plagioclase, orthopyroxene, and clinopyroxene. The later assemblage consists of deformed ortho- and clinopyroxene, accessory ilmenite, plagioclase, quartz, pargasite, and biotite. Plagioclase–orthopyroxene symplectite intergrowths (Fig. 3b) in association with newly formed magnetite are observed at the contact of plagioclase and clinopyroxene grains. Separate grains of late orthopyroxene are also formed beyond the symplectite zone.

In terms of chemical composition, it corresponds to quartz diorite (Table 1) and corresponds to magnesian granitoids. Compared to the average tonalite (Hui et al., 2011; Moyen and Martin, 2012), this rock has two times higher contents of mafic (Fe, Mg, Mn) element and four times higher contents of siderophile elements (Ni + Cr), and have the much lower $(La/Yb)_n = 7.5$) degree of REE fractionation. It is characterized by the absence of Eu anomaly and flat HREE pattern (Fig. 2).

Compositions of minerals in the leuco- and mesocratic enderbite have insignificant differences.

Orthopyroxene of the early assemblage is represented by low-Al ($Al^t = 0.06$) bronzite $En_{52--53}Fs_{46-47}W_1$, #mg = 0.53–0.54, and in the discriminant diagram (Rietmeijer, 1983) falls in the field of metamorphic orthopyroxenes. Late orthopyroxene is more magnesian ($En_{55}Fs_{44}W_1$), and forms both individual grains and lamellae in clinopyroxene.

Clinopyroxene $En_{37-38}Fs_{16-20}W_{47-41}$, #mg = 0.65–0.70 in the diagram Al^{VI}/Al^{IV} (Fig. 4a) is located in the field of the medium- and low-pressure granulite facies. It also occurs in the symplectites.

Compositionally similar orthopyroxene–plagioclase symplectites were described for the Snowbird tectonic zone in the northwestern Canadian shield (Baldwin et al., 2004), where their formation is thought to be related to the exsolution of the *Grt* + *Cpx* + *Pl* assemblage during decompression.

Plagioclase is mainly of intermediate composition (see Supplementary Table EMS1).

According to the classification by Parin et al., (2004), *ilmenite* is ascribed to Fe-rich variety and is partially replaced by titanite and rutile (Fig. 3a).

Amphibole is represented by pargasite (#mg = 0.57–0.60) and Mg-hastingsite (#mg = 0.58–0.65) (Supplementary, Table EMS1, Leake et al., 1978).

Table 1. Element composition of rocks of the composite tectonomagmatic breccia

Element composition	Sample no.						
	UR 82/1a	UR 82/1	UR 82/15	UR 82	UR 82/3	UR 89/16	C10-U4
SiO_2	65.29	60.97	64.5	54.89	55.33	50.61	69.41
TiO_2	0.59	0.52	0.39	0.09	0.25	0.63	0.49
Al_2O_3	13.82	15.13	14.4	2.54	5.24	7.71	13.78
FeOt	7.38	6.94	5.27	15.72	15.11	13.39	3.43
MnO	0.11	0.10	0.08	0.30	0.24	0.26	0.05
MgO	3.99	3.43	4.06	20.85	15.48	13.82	2.09
CaO	4.56	6.95	5.78	3.29	5.15	10.39	3.74
Na_2O	2.77	3.44	3.45	0.12	0.81	1.43	3.38
K_2O	0.60	0.64	0.79	0.10	0.52	0.45	2.10
P_2O_5	0.10	0.16	0.08	<0.01	0.04	0.06	0.14
L.O.I.	<0.1	0.97	0.47	1.15	1.34	0.20	0.47
Sc	14.6	20.6	13.5	9.59	17.5	36.5	5.35
Rb	<2	<2	3.18	2.28	6.13	3.98	39
Sr	371	452	349	11.1	96.3	93.7	337
Y	6.95	13.7	10.5	9.79	17.3	23	6.78
Zr	80.1	115	120	23.0	51.8	18	16
Hf	2.00	–	2.95	0.66	1.51	1.40	3.23
Pb	2.89	2.87	4.35	1.09	1.50	2.20	n.d.
Ba	560	320	504	64	277	105	887
Nb	5.0	2.7	2.0	<0.5	1.49	3.8	2.7
Ta	0.28	0.13	<0.1	<0.1	0.10	0.26	n.d.
Co	26.5	28.5	24.2	77.3	61.0	65.0	10.0
Ni	63.0	89.6	91.8	575	198	355	27
Cr	112	217	347	464	1320	891	58
Zn	80.4	64.6	68.3	162	158	129	23
Cu	28.00	29.2	18.5	6.90	9	27.8	n.d.
V	90.3	131	92.7	23.8	70	248	45
Ga	–	16.1	16.3	5.64	–	11.2	n.d.
Th	0.23	0.13	<0.1	0.29	0.15	0.49	1.28
U	<0.1	<0.1	0.14	<0.1	<0.1	0.04	n.d.
La	36.6	13.5	17.1	2.25	8.13	14.9	16.0
Ce	54.9	26.1	30.1	7.46	18.5	35.3	26.0
Pr	5.31	3.17	3.43	1.29	2.81	5.38	2.65
Nd	17.3	12.9	12.0	5.97	12.3	21.6	9.3
Sm	2.32	2.71	2.06	1.40	3.28	5.46	1.63
Eu	0.96	0.94	0.85	0.14	0.43	0.98	0.88
Gd	2.25	2.67	2.12	1.65	3.05	5.63	1.67
Tb	0.30	0.46	0.34	0.28	0.51	0.89	0.24
Dy	1.32	2.45	1.85	1.75	2.85	5.28	1.29
Ho	0.24	0.49	0.35	0.39	0.64	1.06	0.26
Er	0.78	1.44	1.04	1.09	1.88	2.98	0.79
Tm	0.12	0.18	0.14	0.15	0.25	0.41	0.11
Yb	0.80	1.30	1.04	1.09	1.78	2.64	0.78
Lu	0.12	0.18	0.14	0.19	0.26	0.37	0.11

C10-U4—enderbite, Kazachii Yar quarry (Bibikova et al., 2013). (n.d.) not determined.

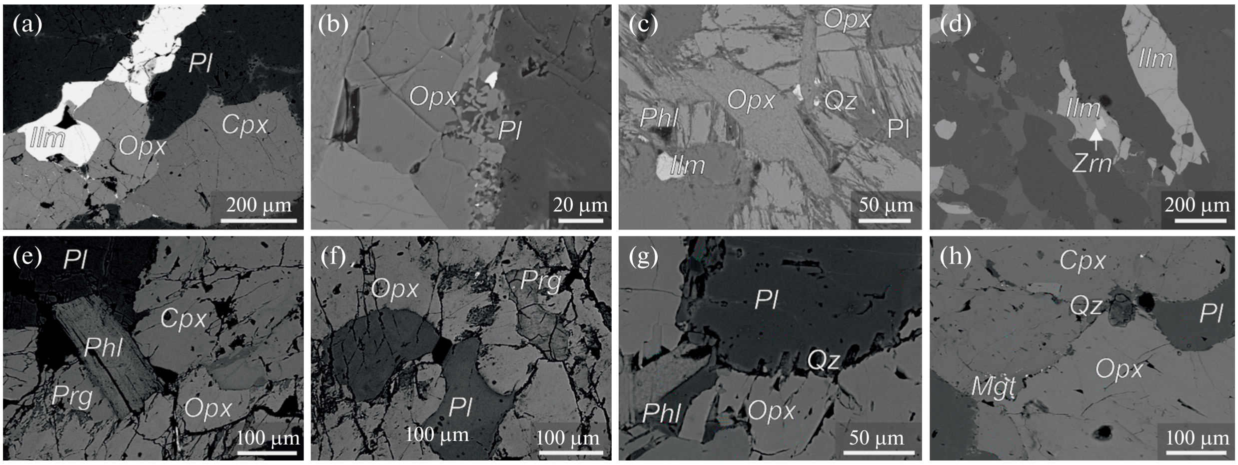

Fig. 3. Back-scattered electron image of mineral relations. (a, b) mesocratic enderbite UR82/1: (a) early assemblage: *Opx*, *Pl*; (b) fragment with *Opx*–*Pl* symplectites; (c, d) leucosome in the enderbite UR82/15: (c) large *Opx* grains with numerous cracks filled with *Qz* and *Pl*; later minerals, Il*m* and *Bt*, (d) large elongated ilmenite crystals in the *Qz*–*Pl* groundmass. Ilmenite contains zircon inclusions; (e, f) coarse-grained metaorthopyroxenite, UR82: (e) sequence of minerals *Opx*–*Cpx*–*Pl*–*Phl*–*Prg*, replaced by actinolite, (f) *Pl*, younger than Opx; contains small grains of altered *Opx*. *Phl* is developed after *Pl*; (g, h) medium-grained metaorthopyroxenite UR82/3: (g) contact between *Pl* and *Opx*. Composition of *Pl* varies from An_{44} in the core to An_{38} in the rims; *Qz* grains are developed at the contact. Platelets of *Phl*, pargasite, and Mg-*Hbl* were formed later than *Opx* and *Pl*; (h) *Opx*–*Cpx*–*Pl* assemblage. Small *Qz* grains are developed at the contact between *Opx* and *Cpx*. Chains of small Cr-*Mgt* grains occur in *Cpx*.

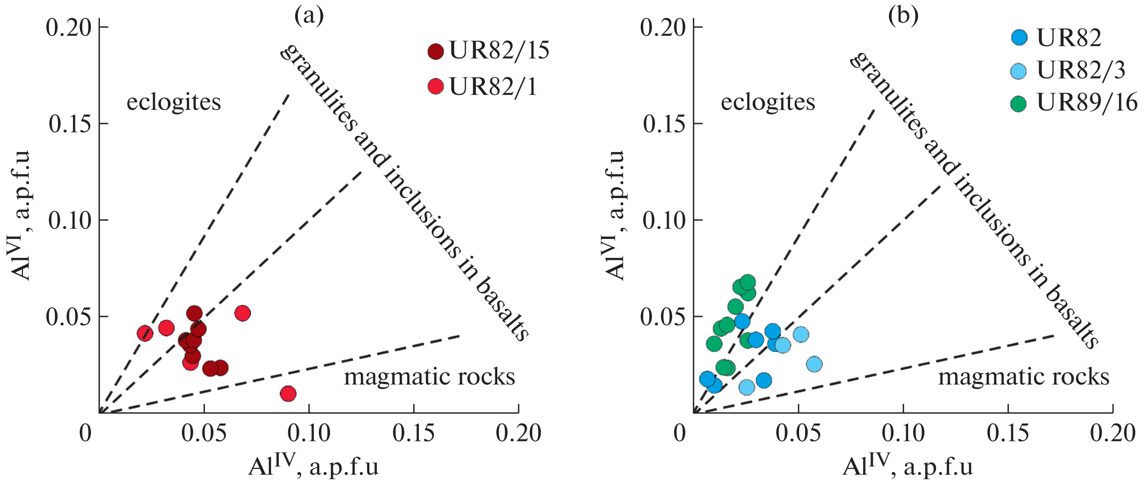

Fig. 4. Position of clinopyroxene from breccia rocks in the diagram Al^{VI} – Al^{IV}. (a) enderbites, (b) metaorthopyroxenites and amphibole–pyroxene schists.

Biotite has varying #mg = 0.51–0.66, high Cr_2O_3 and Cl, low Na_2O contents, and high K/(K + Na) ratio (Supplementary, Table EMS1).

Leucosome in the enderbite (sample UR 82/15) is represented mainly by plagioclase veins 0.5–1.0 cm thick (Fig. 1d). It corresponds to tonalite (Table 1), but differs from the average tonalite–trondhjemite gneiss (Moyen and Martin, 2012) in the flatter REE pattern. Major minerals are andesine and *Qz*, with small amounts (up to 4 vol %) of *Kfs*.

The earliest minerals in the leucosome were preserved as inclusions in the Paleoarchean zircons (grain 7; Fig. 7b, Supplementary, Table EMS1), which are represented by *Pl* ($Ab_{59}An_{40}Or_1$), *Kfs* ($Or_{89}Ab_{11}An_0$), and *Cpx*. Clinopyroxene inclusion contains 0.18–0.62 wt % Cr_2O_3, 0.36–0.49 wt %Na_2O, #mg = 0.71.

Orthopyroxene (Fig. 4a) in the diagram (Rietmeijer, 1983) lies in the fields of metamorphic *Opx* or fall in the transition zone between magmatic to metamorphic *Opx*.

Clinopyroxene #mg = 0.76–0.74, $En_{38}Fs_{13}Wo_{48}$ contains zircon (Fig. 3d). In the diagram Al^{VI}/Al^{IV} (Fig. 4a), its data points fall in the granulite field.

Feldspars are represented by *plagioclase,* which corresponds to andesine and *K-feldspar* $Or_{94-93}Ab_{6-7}$.

Amphibole is represented by magnesiohastingsite and replaces clinopyroxene.

Biotite is frequently secondary (Fig. 3c) with #mg = 0.60–0.59, but occurs only as inclusions in zircon, where it has the higher Fe composition #mg = 0.50.

Coarse-grained metaorthopyroxenite (sample UR82, Fig. 1d) occurs as round enclave 25 × 30 cm in size. Based on the MgO content, it belongs to ultramafic rocks, but has the elevated SiO_2 content, and is characterized by the high HREE, Th, and Ni/Cr >1 (Table 1).

The majority (~90–95%) of the metaorthopyroxenite are made up of coarsely crystalline orthopyroxene (*Opx*1), with less common smaller *Opx2*, as well as *Cpx*, *Pl*, *Phl*, *Amp*, and *Qz*. Composition of *Opx*1 corresponds to bronzite $Ens_{67-69}Fs_{30-32}W_{0-1}$ and plots in the field of metamorphic orthopyroxenes in the diagram (FeO + MgO)–Al_2O_3 (Rietmeijer, 1983). *Opx*2 is formed (Fig. 3e) owing to recrystallization of *Opx*1 with a gradual increase of Mg number up to 0.73.

In the diagram Al^{VI}–Al^{IV}, the *clinopyroxene* falls in the field of the low-grade granulite facies (Fig. 4b). Its recrystallization leads to the formation of higher Mg *Cpx* with higher CaO and lower Na_2O contents.

Plagioclase contains inclusion of *Opx* (Fig. 3f), *Kfs* with *Pl*. The inclusion likely represents crystallized melt, the average composition of which corresponds to a mixture of *Pl* (~95%) and *Kfs* (~5%); *Kfs* is absent in matrix.

Amphibole is represented by pargasite (Fig. 3e), Mg-hornblende, and actinolite.

Phlogopite (Fig. 3e) is locally developed after orthopyroxene containing inclusions of clinopyroxene and amphibole.

Medium-grained metaorthopyroxenite (sample UR82/3) occurs as enclaves 8–10 × 5 cm in size (Fig. 1d), is characterized by the fine to medium-grained massive granoblastic texture. As compared to the metaorthopyroxenite (sample UR82), metaorthopyroxenite UR82/3 distinctly differs in the elevated contents of Al_2O_3, CaO, Na_2O, REE, Y, Zr, Rb, Ba, and Nb (Table 1). As compared to the orthopyroxenites of the Stolzburg layered intrusion (Anhaeusser, 2001) and Monchegorsk pluton (Chashchin et al., 2020), as well as orthopyroxenite enclaves in the Bug complex (Lobach-Zhuchenko et al., 2018), the metaorthopyroxenites UR82 and UR82/3 have lower Mg# owing to the lower MgO content and mainly elevated FeO content.

The early mineral assemblage includes *Opx* (#mg = 0.65), *Cpx*, *Pl* (An_{35-44}); and later assemblage includes *Phl*, *Amp*, and Cr-*Mgt* (Figs. 3g, 3h); the chains of small quartz grains are arranged along pyroxene boundaries. Accessory minerals are *Ap*, Cr-*Mgt*, and *Zrn*.

Orthopyroxene in the diagram FeO + MgO vs Al_2O_3 (Rietmeijer, 1983) is confined to the transitional zone between magmatic and metamorphic orthopyroxenes, and according to the diagram involving calcium (Rietmeijer, 1983) belongs to the metamorphic orthopyroxene.

Clinopyroxene is represented by diopside with #mg = 0.82–0.86. An increase of mg# is accompanied by the decrease of Al and Cr contents and increase of Ca and Si contents.

Plagioclase was formed later than *Opx*, An_{40-44} in the central part of large grains decreases to An_{32-38} in the rims.

K-feldspar is present only as inclusions in zircon; its composition varies from $Ab_{17}An_{11}Ort_{72}$ to Ab_6Ort_{94}.

Later minerals are amphibole and phlogopite (Fig. 3g).

Amphiboles are represented by pargasite (#mg = 0.76–0.78), Mg-hastingsite, and Mg-hornblende with #mg = 0.78–0.84; as well as by anthophyllite–cummingtonite. The amphibole contains small (1–5 mm) inclusions of magnetite with 2 to 4 wt % Cr_2O_3.

Phlogopite contains around 5 wt % TiO_2, #mg = 0.71–0.75, and differs from biotites of other breccia rocks in the high (>1 wt %) Cr_2O_3 content.

Accessory *apatite* is represented by F-apatite formed after phlogopite, with Cl/F = 0.26. Apatites of such composition are not typical of mafic rocks (Bocharnikova et al., 2019), where Cl content is an order of magnitude higher.

Amphibole–pyroxene schist (sample UR89/16) is located in the eastern part of the breccia. It is structurally and compositionally similar to schists located to the north of the breccia (Fig. 1c). It has a fine-grained texture and finely foliated structure with scare quartz–plagioclase veinlets.

Chemically, it corresponds to magnesian basalt that is identical to the adjacent magnesian metabasalts that are intercalated with metakomatiites, tholeiitic basalts, and sediments (Baltybaev et al., 2014). In terms of Th/Ta–La/Yb relations, it is close to submarine flood basalts and basalts of the greenstone belts such as those of the Warawoona block of the Pilbara craton and the Abitibi greenstone belt of the Canadian shield that were derived from a depleted source (Condie, 1994).

Major minerals are amphibole, orthopyroxene, clinopyroxene, plagioclase; accessory minerals (up to 1–2 vol %) are biotite, ilmenite, magnetite, and single grains of dolomite.

Orthopyroxene and *clinopyroxene* form early mineral assemblage surrounded by *Pl*. They were subsequently followed by crystallization of *Ilm*, *Pl* (andesine–oligoclase), *Amp*, and *Phl*. *Cpx* is exsolved into thin *Ilm* and *Opx* lamellae.

Ilmenite in composition is close to those of the Kusa layered gabbro massif (Bocharnikova et al., 2019).

Amphibole is represented by pargasite, #mg = 0.61–0.64, as well as scarce grains of magnesian hornblende with #mg = 0.77–0.78 and TiO_2 = 0.42–1.08 wt %.

Mica is represented by biotite (#mg = 0.63–0.66), which replaces amphibole and contains TiO_2 = 3.9–6.1 wt %.

MORPHOLOGY, INNER STRUCTURE, GEOCHEMISTRY, AND U–Pb AND Lu–Hf ISOTOPE SYSTEMS OF ZIRCONS

The local geochemical and U-Pb isotope studies of zircon were carried out for samples of leucocartic (UR82/1a) and mesocratic (UR82/1) enderbites, leucosomes in enderbites (UR82/15), as well as metaorthopyroxenites (UR82, UR82/3), and crystalline schists (UR89/16/4) of the composite breccia. Zircon from some samples (UR82/1, UR82/15, UR82, and UR89/16) was analyzed for the Lu–Hf isotope composition.

The results of U–Pb and Lu–Hf isotope studies are given in Table 2 and EMS2 in Supplementary materials; the content of trace and rare-earth elements in zircon are given in Table 3. CL images of zircon and obtained U-Pb isotope data are shown in the concordia diagram (Figs. 5, 8).

Leucocratic enderbite UR82/1a. Zircon population is dominated by elongated grains (200 × 600 μm) (Fig. 5a), with CL-dark cores in some grains (domains 2.1, 3.1, 4.1, 5.1); and some grains have equant shape (1.1, 7.1). It is seen that the grains are overgrown by CL-light rim cutting across relict zoning (Fig. 5a).

Isotope U-Pb composition was measured in 15 domains of 11 zircon grains (Table 2). Eight of them gave the $^{207}Pb/^{206}Pb$ age of 3.5–3.62 Ga. The oldest age of 3622 ± 14 Ma was obtained on the upper intercept (at zero lower intercept) for the relicts of the CL lighter domains (domains 6.1re and 6.2re) (Fig. 5a). Close concordant age of 3582 ± 5 Ma was obtained for zoned intermediate zones of zircon (domains 3.2, 6.1) and was calculated for CL-dark cores (2.1, 3.1) at 3573 ± 9 Ma (Fig. 5a).

Concordant $^{207}Pb/^{206}Pb$ ages of 2947 ± 4 and 3064 ± 6 *Ma* were obtained for domains 2.2 and 8.1. Domains 2.2 and 8.1 compared to the domains 6.1 and 3.2 have the lower Th contents (<60 ppm) at close U contents, which resulted in the low (0.11–0.08) Th/U ratio. Domain 2.2 has the lower P, Y, and REE concentrations (Table 3) and smoothed Ce- and Eu-anomalies in the REE distribution patterns compared to the domains with an age of ~3.6–3.5 Ga (2.1, 3.1, 5.1, 6.1, 3.2) (Fig. 6a).

All zircon grains are overgrown by CL-white rims, which overprint dissolution (or melting) traces of the external facets of zircon. Two rims (5.2 and 6.2) gave subconcordant age values, but with higher error: 2090 ± 120 and 2338 ± 89 Ma. The characteristic feature of the rims is the very low contents of U (20–30 ppm) and Th (15–20 ppm) (Table 2).

The REE distribution patterns in zircons from sample 82/1a have a positive Ce* anomaly and insignificant negative Eu* anomaly (Fig. 6a). The highest concentrations of trace elements and REE are typical of domains with an age of around 3.6–3.5 Ga, especially of high-U (1200–3550 ppm) and high-Th (420–1780 ppm) cores (Table 2, Fig. 6a). Equant zircons (1.1, 7.1) with $^{207}Pb/^{206}Pb$ age <2.8 Ga have the lower contents of REE, especially LREE, as well as Ti and Ca. In general, the REE contents decrease with decreasing $^{207}Pb/^{206}Pb$ ages.

Dark cores 2.1 and 5.1 ($^{207}Pb/^{206}Pb$ age over 3.5 Ga, Table 2) having reverse discordance are characterized by the high U and Th contents, which exceed the average values for magmatic and metamorphic zircons (Yakymchuk et al., 2018).

Mesocratic enderbite (UR82/1) contains grains of round and elongated-oval shape, some of which have variably altered CL-dark cores; grains 2, 3, 6 retain relicts of early zoning. The later phase is represented by CL-light rim cutting across relicts of zoning (grains 3, 6, 7, 10, 11) (Fig. 5b).

Isotope U-Pb age was measured and calculated for 20 domains in 13 zircon grains (Table 2). In the concordia diagram, most part of the points plot between values of ~3100 and ~2000 Ma (Fig. 5b). The oldest age of 3104 ± 9 Ma was determined by the upper intercept in zoned zircon grains (domains 1.1, 6.1, and 11.1) (Fig. 5b). The cores are characterized by the moderate contents of U (128–432 ppm) and Th (50–214 ppm) at Th/U ratios of 0.34–0.62 (Table 2), which are typical of magmatic zircons (Yakymchuk et al., 2018). Zircon 6.1 contains large zoned *Opx* inclusion with #mg 0.58 in the core and 0.55 in the rim (Fig. 7a). Close $^{207}Pb/^{206}Pb$ ages of 3.0 and 3.1 Ga were obtained for high-U (~2000 ppm, Th/U = 0.05) cores 10.1 and 12.1 (Table 2, Fig. 5b). However, the latter differ in the lower content of LREE and a more expressed negative Eu anomaly (Fig. 6b). The cores of grain 14 (14.1 and 14.2) gave the lower $^{207}Pb/^{206}Pb$ ages <2.8 Ga and have the extremely high U concentrations (4000–5000 ppm, Th/U = 0.04–0.1) and HREE enrichment (Fig. 6b).

Cores 4.1, 5.1, 7.1, 8.1, 13.1 and domains 1.2, 6.2, and 6.3 with the moderate U content gave discordant age values <2.85 Ga (Table 2), most part of which plot near a 2.95 – 2.0 Ga regression line, while data point 13.1 is close in composition to zircon 7.1 from sample UR82/1a and lies on a 3.6–2.0 Ga regression line (Fig. 5b). The entrapment of core material during the measurement is inferred for the narrow zones 1.2 and 6.2. Domains 1.2, 4.1, 5.1, 11.1 show the lowered Th contents (19–51 ppm).

Zoned cores 2.1 and 3.1 have the low contents of U (30–58 ppm) and Th (35–65 ppm) at high Th/U ratio (1.13–1.15). CL-white rims (6.4, 7.2, and 14.3)

Table 2. U–Th–Pb SHRIMP-II data on zircon from rocks of tectonomagmatic breccia UR82

Analysis no.	U, ppm	Th, ppm	Th/U	$^{206}Pb_c$,[1] %	$^{206}Pb^*$,[2] ppm	$^{207}Pb^*/^{235}U$	±1σ, %	$^{206}Pb^*/^{238}U$	±1σ, %	Rho[3]	Age, Ma				D[4], %
											$^{206}Pb/^{238}U$	1σ	$^{207}Pb/^{206}Pb$	1σ	
Leucocratic enderbite UR82/1a															
1.1	179	70	0.39	0.07	72	10.97	1.0	0.465	0.7	0.70	2460	±15	2570	±12	4
2.1	2255	1781	0.79	0.00	1500	34.39	0.7	0.774	0.6	0.90	3696	±17	3580	±5	–3
2.2	512	58	0.11	0.00	266	19.30	0.8	0.604	0.7	0.87	3047	±17	3064	±6	1
3.1	1215	587	0.48	0.00	744	31.35	0.8	0.712	0.6	0.80	3467	±17	3566	±7	3
3.2	475	269	0.57	0.03	302	33.01	0.7	0.739	0.6	0.87	3566	±17	3589	±5	1
4.1	618	377	0.61	0.04	222	9.62	1.7	0.419	0.6	0.36	2254	±11	2525	±26	12
5.1	3544	421	0.12	0.00	2349	32.43	0.8	0.771	0.6	0.74	3686	±17	3495	±8	–5
5.2	29	19	0.65	1.62	11	9.08	2.8	0.441	2.3	0.40	2357	±45	2338	±89	–1
6.1	435	248	0.57	0.03	275	32.65	0.8	0.737	0.6	0.75	3559	±17	3576	±9	0
6.1RE	148	94	0.63	0.00	93	33.52	1.3	0.736	0.9	0.71	3554	±25	3619	±14	2
6.2	18	14	0.78	2.08	6	6.87	3.9	0.384	2.5	0.33	2097	±44	2090	±120	0
6.2RE	200	107	0.54	0.06	101	26.70	1.7	0.584	1.6	0.95	2967	±39	3623	±9	22
7.1	247	171	0.69	0.04	95	11.90	1.8	0.449	0.7	0.40	2391	±15	2761	±28	15
8.1	657	52	0.08	0.06	325	17.12	1.1	0.576	1.3	0.98	2933	±31	2947	±5	0
9.1	387	226	0.58	0.03	229	29.70	1.2	0.689	1.4	0.98	3378	±35	3532	±4	5
Mesocratic enderbite UR82/1															
1.1	346	214	0.62	0.00	178	19.51	1.5	0.597	1.5	0.96	3018	±35	3100	±7	3
1.2	155	19	0.12	0.03	71	16.31	2.0	0.535	1.5	0.74	2761	±34	2990	±22	8
2.1	30	35	**1.15**	0.00	11	9.99	2.7	0.442	1.8	0.67	2361	±36	2496	±33	6
3.1	58	65	**1.13**	0.35	18	7.37	2.5	0.365	1.8	0.70	2004	±30	2306	±31	15
4.1	167	51	0.30	0.03	73	14.05	2.0	0.507	1.5	0.74	2643	±33	2835	±22	7
5.1	233	33	0.14	–	98	12.71	1.9	0.489	1.4	0.76	2564	±31	2730	±21	6
6.1	432	145	0.34	–	219	19.42	1.5	0.591	1.4	0.96	2993	±34	3109	±7	4
6.2	291	291	1.00	0.03	137	15.53	1.3	0.549	1.2	0.95	2819	±28	2869	±6	2
6.3	124	101	0.82	0.04	48	10.92	1.5	0.450	1.4	0.91	2396	±28	2615	±11	9
6.4	11	12	1.13	0.93	5	12.05	5.4	0.502	2.7	0.50	2623	±59	2596	±78	–1
7.1	413	401	0.97	0.01	180	13.96	1.7	0.508	1.4	0.81	2648	±31	2821	±17	7
7.2	4	3	0.74	–	2	14.30	9.8	0.507	4.3	0.45	2644	±94	2863	±140	8
8.1	560	342	0.61	0.01	240	12.96	1.5	0.498	1.4	0.96	2606	±30	2731	±7	5
10.1	2031	95	0.05	0.01	1040	18.39	1.5	0.595	1.2	0.81	3009	±29	3011	±14	0

Table 2. (Contd.)

Analysis no.	U, ppm	Th, ppm	Th/U	$^{206}Pb_c$,[1] %	$^{206}Pb^*$,[2] ppm	$^{207}Pb^*/^{235}U$	±1σ, %	$^{206}Pb^*/^{238}U$	±1σ, %	Rho[3]	Age, Ma $^{206}Pb/^{238}U$	1σ	$^{207}Pb/^{206}Pb$	1σ	D[4], %
11.1	128	50	0.39	0.02	69	20.23	2.3	0.625	2.1	0.88	3130	±51	3084	±18	–1
12.1	1915	116	0.06	0.00	984	19.58	2.1	0.598	1.2	0.60	3022	±30	3103	±26	3
13.1	347	126	0.36	0.04	139	13.16	1.7	0.466	1.2	0.72	2465	±24	2866	±19	16
14.1	5081	521	0.10	0.00	2460	15.05	1.2	0.564	1.2	0.98	2883	±28	2772	±4	–4
14.2	4320	187	0.04	0.01	1300	8.20	1.5	0.350	1.4	0.92	1933	±24	2559	±10	32
14.3	15	5	0.35	3.12	6	8.33	11.0	0.398	2.6	0.24	2161	±47	2365	±180	9
Leucosome of migmatite UR82/15															
1.1	2061	142	0.07	0.01	993	16.53	2.3	0.561	2.3	0.99	2870	±53	2934	±5	2
1.2	48	93	1.92	0.17	23	14.07	3.3	0.541	2.8	0.85	2789	±63	2729	±29	–2
2.1	41	63	1.52	0.53	13	6.48	4.1	0.362	2.9	0.70	1992	±50	2096	±52	5
3.1	236	150	0.64	0.05	102	13.44	2.5	0.502	2.4	0.95	2621	±52	2779	±13	6
3.2	46	65	1.40	0.27	18	10.69	4.3	0.450	2.9	0.67	2397	±58	2578	±53	8
4.1	71	45	0.63	0.21	30	12.71	3.2	0.492	2.7	0.86	2579	±58	2720	±27	5
5.1	679	272	0.40	0.00	347	19.97	2.6	0.596	2.3	0.90	3012	±56	3141	±18	4
6.1	27	16	0.58	1.61	8	4.90	8.9	0.329	3.5	0.40	1832	±56	1769	±150	–3
7.1	1092	90	0.08	0.03	366	8.22	2.4	0.390	2.3	0.96	2121	±42	2379	±12	12
7.2	171	112	0.65	0.08	64	10.00	3.6	0.438	2.4	0.68	2342	±48	2513	±45	7
8.1	3456	154	0.04	0.01	1790	22.19	1.3	0.602	1.3	0.97	3037	±32	3291	±6	8
8.2	2540	133	0.05	0.01	1300	18.90	1.5	0.598	1.3	0.90	3021	±32	3048	±10	1
9.1	1189	40	0.03	–	481	14.06	1.6	0.471	1.4	0.87	2488	±28	2955	±12	19
9.2	2767	178	0.06	0.01	1200	13.85	1.5	0.504	1.3	0.89	2632	±29	2819	±11	7
Metaorthopyroxenite UR82															
1.1	137	100	0.73	0.00	67	15.13	1.8	0.566	1.7	0.93	2891	±39	2776	±10	–4
2.1	213	123	0.58	0.00	69	7.01	1.9	0.375	1.5	0.82	2050	±27	2173	±18	6
2.2	356	149	0.42	0.02	122	7.75	1.7	0.398	1.5	0.86	2160	±28	2242	±15	4
2.3	93	86	0.93	–	31	7.19	2.4	0.385	1.7	0.70	2097	±30	2172	±30	4
3.1	155	61	0.40	0.05	62	11.51	2.7	0.465	1.6	0.57	2461	±32	2649	±37	8
4.1	193	108	0.56	0.02	76	11.37	2.0	0.454	1.5	0.76	2412	±31	2668	±22	11
5.1	196	105	0.54	0.05	104	22.57	1.6	0.616	1.5	0.95	3095	±38	3281	±8	6
6.1	162	66	0.41	–	96	28.03	1.7	0.688	1.6	0.92	3377	±41	3446	±11	2
7.1	1007	267	0.27	0.01	617	29.84	1.5	0.713	1.5	0.98	3471	±41	3487	±4	0

Table 2. (Contd.)

Analysis no.	U, ppm	Th, ppm	Th/U	$^{206}Pb_c$,[1] %	$^{206}Pb^*$,[2] ppm	$^{207}Pb^*/^{235}U$	±1σ, %	$^{206}Pb^*/^{238}U$	±1σ, %	Rho[3]	Age, Ma				D[4], %
											$^{206}Pb/^{238}U$	1σ	$^{207}Pb/^{206}Pb$	1σ	
7.2	95	55	0.58	0.36	40	12.50	3.7	0.488	1.7	0.44	2563	±35	2705	±55	6
7.3	924	249	0.27	0.01	471	24.52	4.1	0.594	1.5	0.37	3004	±36	3468	±59	15
8.1	52	65	1.26	0.10	23	13.05	2.0	0.508	1.6	0.81	2649	±35	2710	±19	2
9.1	1272	164	0.13	0.02	553	15.82	1.4	0.506	1.4	0.97	2639	±30	3029	±6	15
10.1	570	343	0.60	0.02	234	12.05	1.7	0.477	1.6	0.95	2513	±34	2684	±8	7
Metaorthopyroxenite UR82/3															
1.1	104	481	4.60	0.11	46	17.23	1.9	0.510	1.5	0.79	2657	±33	3153	±19	19
2.1	121	487	4.02	0.06	39	7.49	1.8	0.373	1.5	0.82	2046	±26	2292	±18	12
3.1	518	212	0.41	0.04	223	13.48	1.9	0.500	1.4	0.75	2613	±31	2790	±21	7
4.1	94	413	4.40	0.15	29	6.79	2.1	0.360	1.6	0.78	1980	±28	2189	±23	11
5.1	182	1080	5.92	0.13	54	6.55	2.6	0.343	1.5	0.56	1898	±24	2210	±38	16
6.1	1111	268	0.24	0.01	456	12.55	1.5	0.478	1.4	0.94	2518	±29	2746	±8	9
6.2	59	59	1.00	0.00	26	12.13	3.2	0.523	1.7	0.53	2711	±38	2541	±45	–6
7.1	74	264	3.59	0.00	33	16.05	1.8	0.526	1.6	0.86	2726	±35	2989	±15	10
8.1	767	134	0.17	0.00	484	34.58	1.4	0.734	1.4	0.98	3548	±38	3670	±5	3
9.1	88	298	3.40	–	32	10.78	1.9	0.430	1.6	0.81	2305	±30	2670	±19	16
Amphibole–pyroxene crystalline schist UR89/16															
1.1	528	626	1.18	0.07	212	11.89	2.6	0.467	2.3	0.88	2471	±48	2694	±20	9
2.1	206	95	0.46	0.04	105	21.04	2.7	0.591	2.4	0.89	2992	±58	3237	±20	8
2.2	101	72	0.72	0.01	66	26.31	2.9	0.765	2.6	0.91	3663	±74	3181	±19	–13
3.1	452	57	0.13	0.03	193	12.83	2.9	0.497	2.3	0.80	2601	±50	2718	±29	5
4.1	177	114	0.64	0.04	83	17.90	2.6	0.543	2.4	0.95	2795	±55	3114	±12	11
5.1	157	194	1.23	0.12	60	10.59	2.6	0.442	2.4	0.94	2358	±47	2595	±15	10
6.1	267	79	0.30	0.05	131	20.35	2.9	0.571	2.4	0.81	2913	±56	3237	±27	11
6.2	114	25	0.22	0.00	50	15.31	1.7	0.517	1.5	0.87	2685	±33	2943	±14	10
7.1	127	106	0.83	0.00	58	14.55	2.7	0.532	2.4	0.91	2751	±54	2812	±18	2
7.2	62	34	0.55	0.29	29	14.40	3.8	0.535	2.6	0.69	2764	±58	2786	±44	1
8.1	294	90	0.31	0.03	175	29.62	2.4	0.692	2.3	0.98	3391	±61	3523	±7	4
9.1	247	75	0.31	0.16	109	14.91	1.6	0.510	1.5	0.89	2655	±32	2922	±12	10

[1] Pb_c – common lead with correction for measured ^{204}Pb; composition of common lead was taken according to Stacey–Kramers model (Stacey and Kramers, 1975). [2] Pb^* – radiogenic lead. [3] *Rho* is the error correlation coefficient of Pb/U ratios. [4] D – discordance, %.

Table 3. Geochemical composition of zircon from the rocks of tectonomagmatic breccia UR82 (ppm)

Spot	La	Ce	Pr	Nd	Sm	Eu	Gd	Dy	Er	Yb	Lu	P	Ca	Ti	Y	Nb	Hf	REE	HREE	Eu/Eu*	Ce/Ce*	(Lu/Gd)$_n$	T, °C
Leucocratic enderbite UR82/1a																							
1.1	0.06	5.93	0.04	0.36	0.44	0.18	3.38	18.3	51.6	129	26.7	67.8	1.62	8.11	251	7.87	9562	236	229	0.46	30	65	723
2.1	0.09	44.3	0.17	2.63	5.68	0.49	34.6	152	365	690	119	598	4.34	32.7	1879	17.4	9983	1414	1361	0.11	87	28	857
2.2	0.21	4.34	0.24	1.76	1.13	0.50	5.84	29.5	80.8	177	32.4	60.0	9.24	13.7	406	11.5	11078	334	325	0.60	4.7	46	769
3.1	3.10	20.2	0.63	3.88	3.43	0.79	18.4	81.7	200	377	66.0	206	38.4	11.9	1001	6.49	10536	774	742	0.30	3.5	29	756
3.2	0.51	32.4	0.64	5.43	4.98	1.07	23.9	95.3	232	416	72.3	205	17.5	12.1	1153	6.19	8733	885	840	0.30	14	25	758
5.1	1.59	25.1	1.34	7.28	3.94	1.02	18.5	100	287	677	123	354	12.5	28.6	1398	15.8	11604	1246	1206	0.37	4.2	55	843
6.1	1.54	25.5	0.62	4.07	2.72	0.49	12.2	44.0	109	203	33.2	256	155	17.2	628	0.12	8834	436	401	0.26	6.4	22	791
7.1	0.07	19.9	0.04	0.64	1.93	0.24	13.4	62.9	147	297	53.3	182	0.87	5.10	775	7.54	9931	597	574	0.15	92	33	685
Mesocratic enderbite UR82/1																							
1.1	0.19	39.2	0.13	1.65	4.55	2.15	28.0	108	248	484	81.9	198	15.4	18.4	1325	17.4	8569	997	950	0.58	62	24	798
1.2	0.05	7.54	0.05	0.74	1.28	0.17	6.74	26.8	57.8	109	17.5	97.1	0.13	8.66	338	10.6	8398	228	218	0.18	37	21	728
3.1	0.04	9.34	0.06	0.57	0.67	0.17	2.65	12.5	33.3	73.7	13.8	69.8	1.20	6.58	166	12.1	8350	147	136	0.38	48	43	706
4.1	0.02	7.14	0.02	0.57	1.33	0.44	7.74	36.5	99.7	221	47.3	234	0.60	9.61	498	10.9	10970	422	412	0.42	86	50	737
5.1	0.13	5.06	0.15	1.40	1.43	1.39	9.11	46.2	147	324	61.2	131	9.00	6.11	748	9.47	7728	597	587	1.18	8.9	55	699
6.1	0.07	11.7	0.06	0.81	3.04	1.02	18.3	68.1	154	299	52.9	106	7.35	12.4	839	12.6	8459	609	592	0.42	44	24	760
6.3	0.11	11.2	0.11	0.79	0.91	0.21	3.82	15.8	46.0	103	19.2	50.8	5.59	18.9	256	13.5	9511	201	188	0.35	26	41	800
6.4	0.04	8.74	0.03	0.35	0.60	0.11	3.70	15.0	35.0	66.7	12.8	88.3	0.99	13.8	234	8.25	8184	143	133	0.22	69	28	770
7.1	0.02	14.7	0.05	0.64	0.99	0.31	6.31	31.1	86.5	193	36.6	167	1.96	18.0	467	10.6	9446	370	354	0.38	116	48	796
7.2	0.02	7.73	0.03	0.50	0.91	0.13	5.02	21.2	47.3	89.0	15.4	104	0.58	18.6	270	12.0	8517	187	178	0.19	71	25	799
10.1	0.04	8.25	0.05	0.37	0.70	0.08	4.84	28.9	91.5	265	60.5	184	0.85	62.1	489	8.03	16112	460	451	0.13	46	103	932
11.1	0.14	9.71	0.13	1.70	2.38	0.80	11.0	45.1	109	235	43.1	96.1	4.45	11.2	532	13.3	9026	459	444	0.48	18	32	751
12.1	0.15	8.73	0.10	0.77	1.01	0.21	8.38	54.1	148	295	50.4	268	5.80	47.1	755	12.9	12772	567	556	0.22	18	49	898

Table 3. (Contd.)

Spot	La	Ce	Pr	Nd	Sm	Eu	Gd	Dy	Er	Yb	Lu	P	Ca	Ti	Y	Nb	Hf	REE	HREE	Eu/Eu*	Ce/Ce*	(Lu/Gd)$_n$	T, °C
14.1	0.13	13.9	0.07	0.79	2.69	1.04	17.7	115	237	505	88.4	484	3.97	39.6	1512	8.45	8491	982	963	0.46	36	41	878
14.3	0.06	4.80	0.08	0.69	0.87	0.16	3.25	13.2	30.5	61.9	10.9	48.3	15.4	7.59	171	6.90	9057	126	120	0.28	17	28	717
Migmatite leucosome UR82/15																							
1.1	0.10	5.98	0.03	0.31	0.60	0.08	7.59	79.9	339	1173	213	516	1.92	48.7	1413	84.6	17693	1820	1813	0.11	25	230	902
1.2	0.13	14.3	0.09	0.83	0.98	0.27	5.54	22.5	58.6	135	25.1	106	95.5	15.5	309	36.6	9898	263	246	0.35	33	37	781
2.1	0.07	13.2	0.12	0.98	0.99	0.26	4.48	17.7	43.9	97.9	17.6	78.3	44.9	11.6	235	20.7	9422	197	182	0.38	35	32	754
3.1	0.07	15.1	0.07	0.92	1.47	0.32	10.2	40.2	95.3	190	34.3	129	2.63	7.93	530	18.0	9736	388	370	0.25	52	28	721
3.2	0.03	11.2	0.04	0.43	0.76	0.12	3.66	14.8	41.8	93.0	15.6	91.7	2.81	11.3	211	17.9	9109	182	169	0.22	77	35	752
4.1	0.07	9.32	0.05	0.57	0.96	0.16	6.20	25.6	59.1	98.7	17.2	116	11.5	8.78	311	13.2	8668	218	207	0.20	40	23	730
5.1	0.37	10.7	0.32	2.39	3.23	1.66	23.0	96.4	222	376	63.3	133	4.13	15.6	1206	23.9	7489	799	781	0.59	7.6	23	782
6.1	0.15	11.4	0.10	1.09	1.33	0.25	6.96	25.9	52.7	91.0	14.7	122	23.7	8.92	308	26.4	9362	206	191	0.25	23	17	731
7.1	3.16	30.9	3.37	20.4	8.09	4.41	15.2	42.4	142	450	91.7	249	33.5	17.4	724	58.1	16215	812	741	1.21	2.3	49	792
7.2	0.09	11.8	0.13	0.78	0.90	0.17	4.07	18.4	50.3	106	18.4	95.6	12.1	9.32	248	33.3	10457	210	197	0.27	27	37	735
Metaorthopyroxenite UR82																							
1.1	0.08	12.8	0.08	0.91	1.83	0.27	9.71	35.6	78.5	149	26.0	159	0.92	9.02	506	36.7	7752	315	299	0.19	41	22	732
2.2	0.07	19.1	0.11	0.90	2.10	0.36	14.1	70.9	183	396	70.2	344	0.17	7.85	941	39.3	9745	757	735	0.20	53	41	720
2.3	0.11	24.9	0.17	1.48	1.88	0.32	8.83	31.5	69.7	146	24.0	124	0.91	5.22	391	30.4	8196	309	280	0.24	45	22	687
3.1	0.06	9.50	0.04	0.42	0.91	0.17	5.56	22.0	53.2	111	20.3	100	0.96	9.16	299	14.8	8282	223	212	0.23	47	30	733
5.1	0.37	11.3	0.12	1.07	2.01	0.51	14.5	68.9	149	286	46.1	148	38.9	7.84	894	26.3	7711	579	564	0.29	14	26	720
6.1	0.06	9.01	0.04	0.36	1.02	0.20	7.13	33.8	87.3	184	31.5	98.2	5.17	10.5	487	33.7	7745	354	343	0.22	46	36	745
7.1	0.05	19.5	0.11	1.49	3.06	0.44	15.5	74.5	198	456	79.7	353	47.7	9.79	1156	20.0	11350	848	823	0.20	66	42	739
7.2	0.23	8.46	0.08	0.59	1.01	0.26	5.43	21.9	51.3	105	18.5	40.4	41.2	4.43	301	16.9	8745	213	202	0.33	15	28	674

Table 3. (Contd.)

Spot	La	Ce	Pr	Nd	Sm	Eu	Gd	Dy	Er	Yb	Lu	P	Ca	Ti	Y	Nb	Hf	REE	HREE	Eu/Eu*	Ce/Ce*	(Lu/Gd)$_n$	*T*, °C
8.1	0.08	12.5	0.07	0.67	1.30	0.34	8.28	34.8	86.9	174	30.8	111	4.10	6.39	471	17.3	8468	350	335	0.32	41	31	703
9.1	0.09	13.3	0.07	0.71	1.22	0.42	6.77	34.7	103	277	49.9	154	7.56	8.38	598	25.2	12121	487	471	0.44	41	61	726
Metaorthopyroxenite UR82/3																							
1.1	0.06	41.5	0.38	6.02	10.5	1.81	51.1	155	230	303	45.4	323	5.14	11.0	1609	10.6	7558	845	785	0.24	67	7.3	750
3.1	0.12	26.6	0.13	1.84	4.92	0.33	33.4	166	385	756	127	826	2.43	18.8	2130	16.3	9499	1502	1468	0.08	51	31	800
4.1	0.31	35.9	0.54	8.06	10.0	2.28	45.5	136	211	288	45.0	418	32.4	6.32	1467	12.8	7940	782	725	0.33	22	8.1	702
6.1	0.04	28.3	0.05	1.04	3.41	0.20	26.7	150	361	723	124	589	1.32	21.5	2036	30.1	10419	1418	1385	0.06	150	38	813
6.2	0.07	14.1	0.04	0.42	0.86	0.13	4.63	21.1	49.0	100	18.1	118	3.18	6.54	278	4.03	8563	209	193	0.20	67	32	705
8.1	0.10	18.9	0.17	2.56	4.48	0.45	26.7	111	258	474	80.7	298	2.36	19.5	1421	10.1	8496	978	951	0.13	36	25	803
9.1	0.05	38.5	0.23	4.22	7.79	1.32	35.2	128	225	308	47.7	282	0.95	5.42	1443	10.2	8010	796	744	0.24	85	11	690
Amphibole–pyroxene schist UR89/16																							
1.1	0.32	30.7	0.34	2.65	3.39	1.09	18.2	65.2	145	252	43.9	179	5.37	15.0	812	9.84	10221	563	525	0.42	23	20	778
2.1	0.04	7.47	0.02	0.49	1.04	0.26	7.00	35.0	89.2	209	41.1	113	0.26	12.3	484	12.5	9077	390	381	0.29	67	48	760
2.2	0.03	9.09	0.03	0.41	0.85	0.21	3.83	14.6	36.4	76.9	14.0	66.5	0.42	13.7	193	8.61	9158	156	146	0.36	66	30	769
3.1	0.03	3.18	0.02	0.14	0.59	0.29	5.70	37.7	134	355	71.9	215	0.47	9.12	631	6.63	10578	609	604	0.48	31	103	733
4.1	0.03	8.02	0.03	0.31	0.68	0.12	4.90	24.5	69.8	159	30.1	78.4	0.68	11.5	360	6.49	10027	298	288	0.20	62	50	753
5.1	0.17	16.5	0.22	2.36	3.00	0.71	13.0	40.8	84.7	155	27.5	108	3.92	8.50	481	11.6	9079	344	321	0.34	21	17	727
6.1	0.03	4.88	0.04	0.30	0.55	0.13	3.19	13.9	41.9	97.7	19.5	52.8	0.91	7.83	213	10.5	9246	182	176	0.31	34	50	720
6.2	0.06	5.77	0.06	0.52	0.77	0.16	4.59	22.2	60.6	126	24.8	103	8.68	5.50	348	6.09	8965	245	238	0.26	24	44	691
7.1	0.05	3.96	0.03	0.29	0.56	0.25	3.92	15.9	39.8	84.1	16.5	33.3	0.55	7.74	213	4.79	6378	165	160	0.52	26	35	719
7.2	0.02	2.72	0.02	0.06	0.19	0.14	1.19	6.10	15.9	40.1	7.63	41.2	2.38	7.03	83	9.47	6730	74	71	0.90	37	53	711
8.1	0.09	2.62	0.03	0.34	0.67	0.22	5.23	21.6	59.6	134	26.0	87.9	1.32	22.4	303	9.53	7588	250	246	0.35	13	41	817

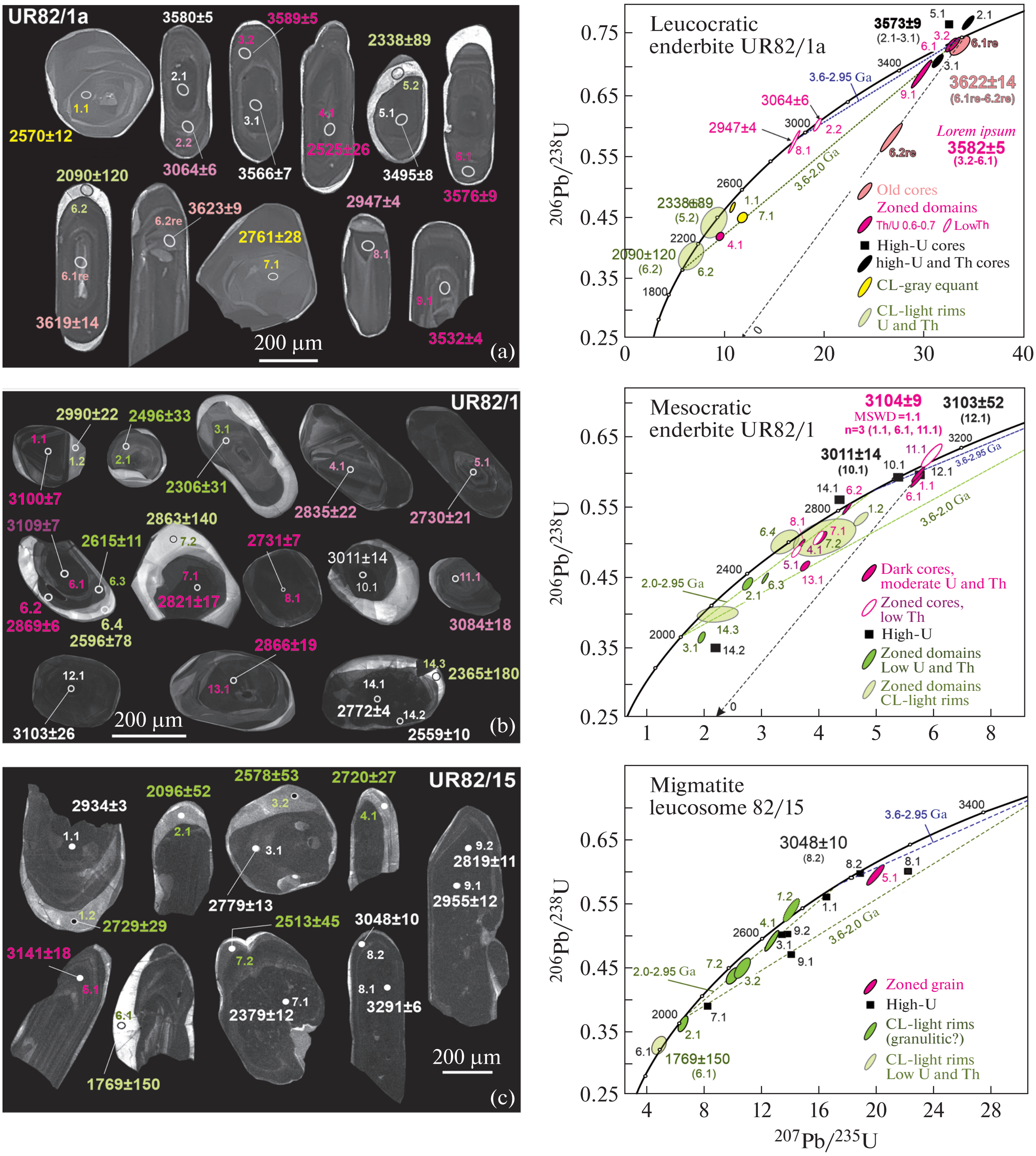

Fig. 5. Cathodoluminescence images of zircon and concordia diagrams. (a) from leucocratic enderbite UR82/1a, (b) mesocratic enderbite UR82/1, (c) leucosome UR82/15. Point numbers in the U–Pb dagrams correspond to point numbers in the cathodoluminescence zircon images, with indication of ^{207}Pb/^{206}Pb age near point number. Age is given in Ma. Subsidiary regression lines are shown: 3.6–2.0, 3.6–2.95, and 2.95–2.0 Ga.

have similar composition, but differ in the lower contents of U (4–15 ppm) and Th (5–12 ppm). Age estimates obtained for rims have the greater error. Zircon with the low contents of U and Th (core 3.1, zones 1.2, 6.2, and rims 6.4, 7.2, and 14.3) shows the lowered content of REE, especially HREE (Table 3, Fig. 6b).

High-U zircon cores with the oldest concordant ages of 3011 ± 14 (10.1) and 3103 ± 52 (12.1) Ma have the lowest $^{176}Hf/^{177}Hf_{(0)}$ = 0.28055 and 0.28058, $\varepsilon_{Hf}(t)$ = –11.6 and –8.2 and $t_{(Hf)}DM$ = 3.69 and 3.65 Ga, respectively (EMS2). Zircon 11.1 with the moderate U content and age of 3104 ± 9 Ma have

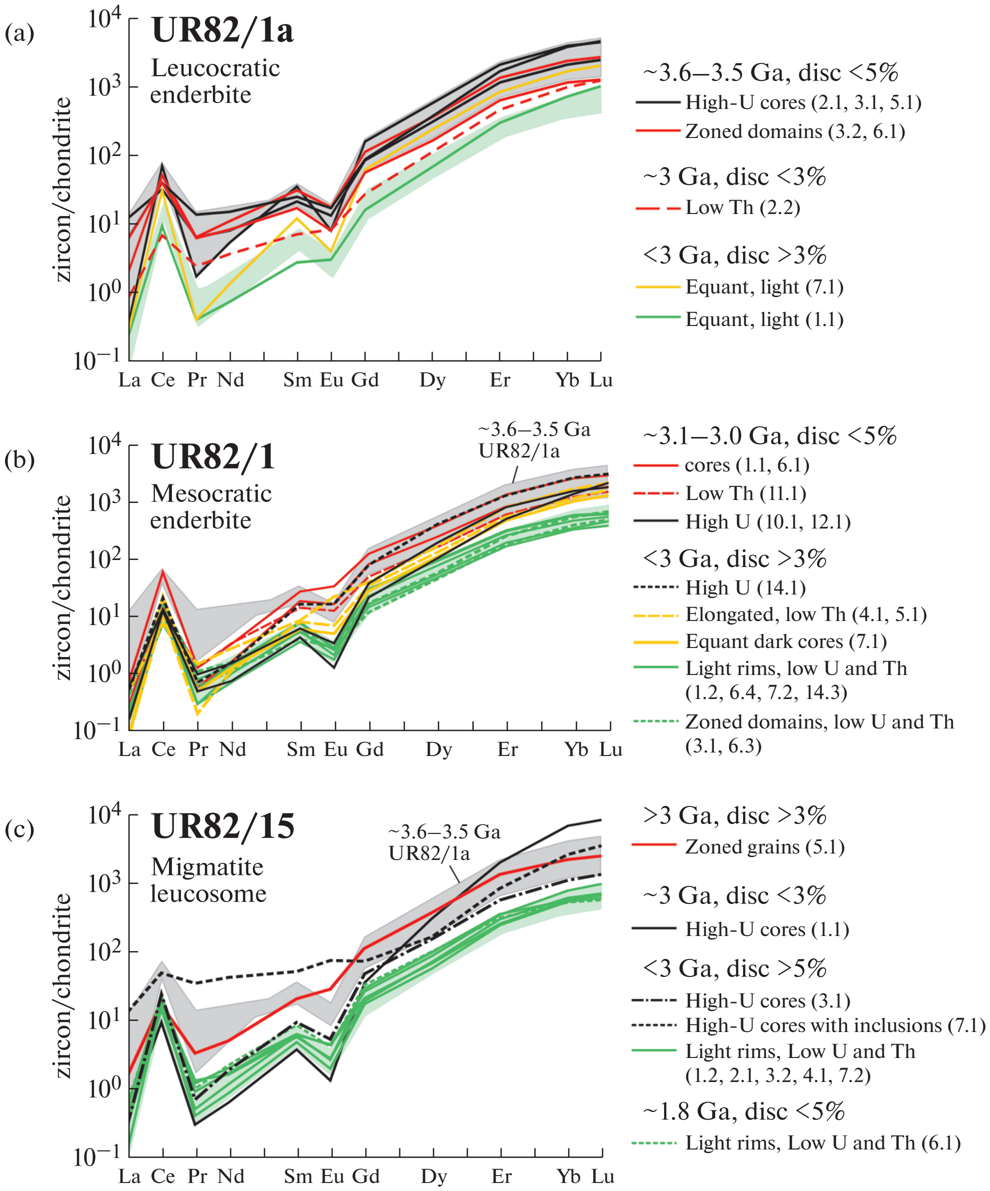

Fig. 6. Chondrite-normalized (Sun and McDonough, 1989) REE distribution pattern in zircon. (a) from leucocratic enderbite UR82/1a, (b) mesocratic enderbite UR82/1, (c) leucosome UR82/15.

$^{176}Hf/^{177}Hf_{(0)} = 0.28065$ and $\varepsilon_{Hf}(3.1) = -5.3$ (EMS2). Close measured isotope ratios of $^{176}Hf/^{177}Hf_{(0)} = 0.28063$ were determined in the zircon cores (7.1, 8.1), which have discordant $^{207}Pb/^{206}Pb$ ages.

Zircon cores 5.1, 14.1, and 14.2 have the higher measured $^{176}Hf/^{177}Hf_{(0)} = 0.28082–0.28095$, which is correlated to the elevated HREE contents.

Zircon from **enderbite leucosome** UR82/15 is mainly represented by prismatic grains from 200 to 900 μm in size (Fig. 5c), which are similar to those of the leucoenderbite UR82/1a. Dark brown cores are surrounded by pink or yellowish rims. Colored zircons also form independent crystals with sectorial zoning. Dark cores with gray and light rims are seen in CL images. The cores contain numerous inclusions of *Kfs*, *Pl*, *Ap*, *Qz*, more rarely *Bt*, *Hbl*, *Cpx*, *Mgt* and their intergrowths; which is a distinctive feature of leucosome zircon.

U–Pb dating was carried out for 14 domains from 9 zircon grains (Fig. 5c, Table 2). The oldest grains (domains 8.1 and 9.1) have the highest U content (1189–3456 ppm) and low Th/U ratio (0.03–0.04). Together with the core of similar composition and structure (7.1), they are arranged along the 3.6–2.0 Ga regression line (Fig. 5c). The central portions of these grains are saturated in *Kfs*, *Pl*, and *Ap* inclusions and their intergrowths (Figs. 5c, 7b). Grain 7 has a com-

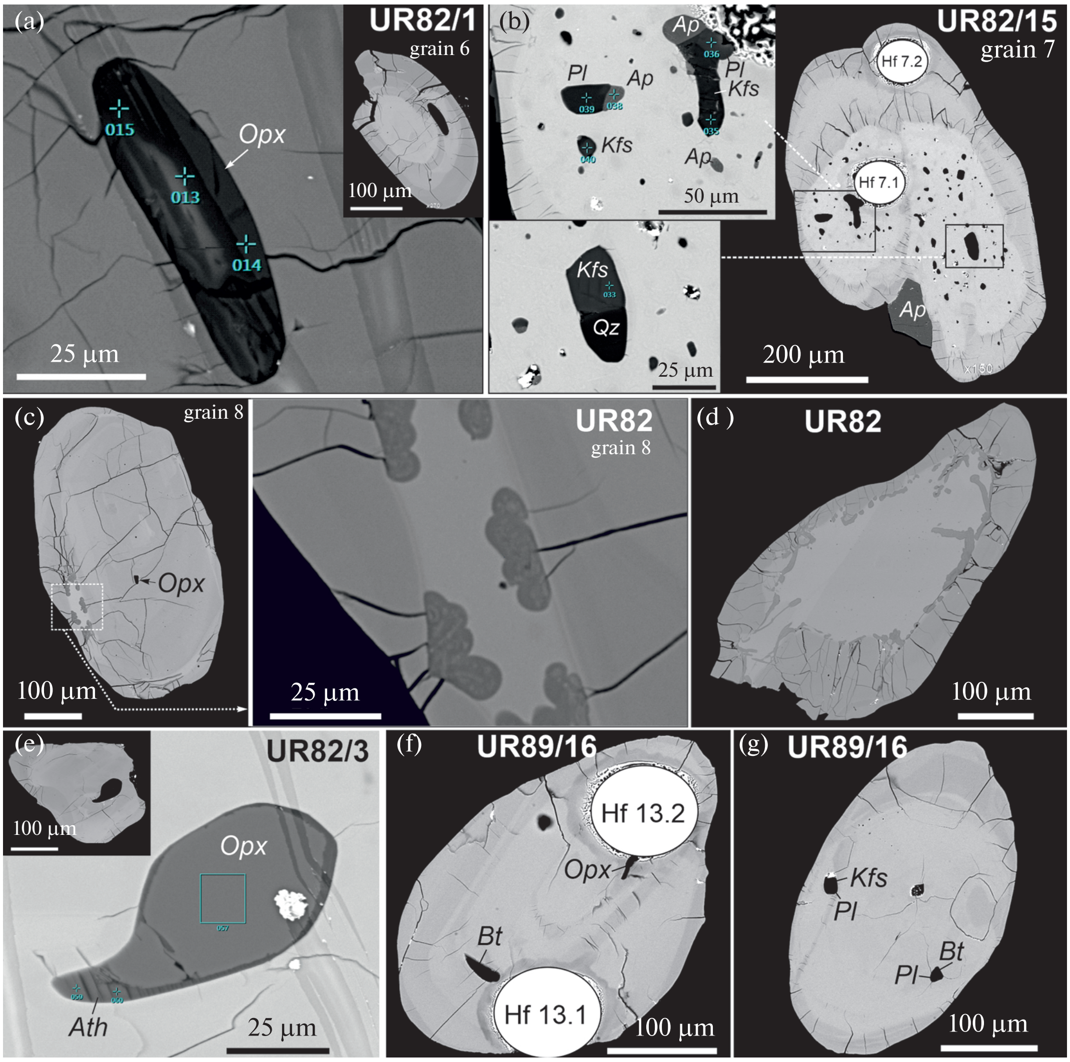

Fig. 7. Microphotos (BSE) of inclusions and alteration zones in the zircon grains from breccia rocks UR82. (a) *Opx* zoned inclusion in zircon from mesocratic enderbite UR82/1, (b) zircon from leucosome UR82/15 with numerous inclusions of *Kfs*, *Pl*, *Ap*, *Qz*, *Bt*, *Hbl*, *Cpx*, *Mgt* and their intergrowths, (c, d) replacement of fractured zones by newly formed zircon in the zircon grains from orthopyroxenite UR82, (e) *Opx* inclusion in anthophyllite rim in zircon from orthopyroxenite UR82/3, (f, g) mineral inclusions in zircons from amphibole–pyroxene schist UR89/16.

posite structure, representing two intergrown prismatic grains rimmed by microinclusion-free CL-lighter rim (Fig. 7b). The grain rim 8.2 yields a concordant age of ~3 Ga (Table 2).

High-U zircon domains (1.1, 3.1, 9.2) and CL-gray rim of different thickness (spots 1.2, 2.1, 3.2, 4.1, and 7.2) have discordant age values. In Fig. 5c, they plot on a 2.95–2.0 Ga regression line.

Many zircon grains have thin CL-white continuous or discontinuous rims, which replace gray rims (Fig. 5c). White rim (zircon 6.1) has very low U (27 ppm) and Th (16 ppm) contents; it defines a subconcordant age with a great error: 1769 ± 150 Ma. It should be noted that the age of the low-U young rim in all considered samples was determined with a great error, which is related to the extremely low content of radioactive elements.

High-U domains 1.1, 7.1, 3.1, 8.2, and 9.2 differ in the low Th/U ratio (0.03–0.08) and high Nb, Hf, Y, Ti, and P concentrations (Tables 2, 3). Domain 7.1 due to the mineral inclusions has the lower U, Th, REE, and Y contents and elevated LREE contents, as well as smoothed Eu and Ce anomalies (Table 3, Fig. 6c). Zircon 5.1 with Pb^{207}/Pb^{206} age of 3143 ± 18 Ma plots on the concordia diagram near zircons from samples UR82/1 (1.1, 6.1, 12.1) and UR82/1a (2.2) with an age of ~3.1–3.0 Ga and likely, is ascribed to the same group, has high Y content, low (7.6) Ce*, which records low fO_2. Zircon rims have the low U and Th concentrations (usually <100 ppm) at elevated Th/U ratio (up to 1.9) (Table 2), contents of REE, especially

HREE, as well as well-expressed Ce and Eu anomalies in the REE distribution patterns (Fig. 6c).

Most part of analyzed zircon grains is characterized by the low measured $^{176}Hf/^{177}Hf_{(0)} = 0.28046–0.28062$ and calculated values of $t_{(Hf)}DM = 3.8–3.6$ Ga, while single domains have the elevated ratios of 0.28070–0.28090 (Supplementary, Table EMS2). The lowest $^{176}Hf/^{177}Hf_{(0)} = 0.28046–0.28051$ were determined in the old high-U zircon cores (points 8.1 and 9.1) and undated cores of zircons 4 (core) and 6 (core), with calculated $t_{(Hf)}DM = 3.82–3.76$ Ga.

The hafnium isotope age of rims of old grains and light low-U rims with Pb^{207}/Pb^{206} age <3.1 Ga (points 2.1, 3.2, 4.1, 6.1, 7.2, 8.1.1, 8.2, 9.2) differs in the insignificant increase of $^{176}Hf/^{177}Hf_{(0)} = 0.28055–0.28062$.

Some zircon grains (1.1, 2, 3.1, 7.1, 5.1, 10.2, 13, 14) gave elevated $^{176}Hf/^{177}Hf_{(0)} = 0.28062–0.28090$, which correlate with high $^{176}Lu/^{177}Hf > 0.0007$ and $^{176}Yb/^{177}Hf > 0.015$, as well as total HREE. Many of these grains are saturated in *Kfs*, *Pl*, *Bt*, and *Ap* inclusions.

Metaorthopyroxenite UR82. Zircon is represented by brown and pink grains of diverse shape and structure. Compared to zircon from enderbites, its grains are more diverse in size and shape, with the predominance of large grains (Fig. 8a). In CL images, we observe oval grains with relicts of oscillatory zoning (zircons 1, 3, 8); and elongated larger grains (>1000 μm) with relicts of faces, oscillatory, and sectorial (5, 6) zoning; as well as dark fragments with gray and white rims (7, 9, 10), and dark cores with thick gray rim (2, 4) (Fig. 8a). Many grains contain inclusions. In some grains, the most fractured zones are replaced by the newly formed zircon (Figs. 7c, 7d).

U–Pb isotope age was measured and calculated for 14 domains from 10 zircon grains. In the U–Pb concordia diagram (Fig. 8a), the oldest Pb^{207}/Pb^{206} ages of ~3.5 Ga were obtained for high-U (U ~ 1000 ppm) grain 7 (domains 7.1, 7.3) and grain 6.1 (Table 2). Grain 9, similar to grain 7, lies on a ~3.5–2.0 Ga regression line.

Other analyzed zircon domains have discordant age values, most part of which, regardless of the composition and structure (including CL-light rims with low REE, U, and Th contents), on Fig. 8a plot near a 2.95–2.0 Ga regression line. The characteristic feature of all zircon types from metaorthopyroxenite UR82 is a homogenous REE distribution, which is similar to that of mesocratic enderbite UR82/1 (Fig. 9a).

Zircon 8 contains orthopyroxene inclusion (Fig. 7c) with #mg 0.72, corresponding to orthopyroxene of late generation. In the rim, this zircon grain is replaced by lamellae of newly formed zircon with trace Fe, Al, Mn, Ca, and Na. The same domains frequently contain inclusions of *Kfs*, *Pl*, *Opx*, and *Amp*.

In CL, grain 2 has a thick light heterogeneous rim and a darker spotted core. Domains 2.1, 2.2, and 2.3 have close Pb^{207}/Pb^{206} age around 2 Ga (Table 2). The darker domain of the core (point 2.2) have the higher contents of U and Th (356 and 149 ppm) and HREE (Table 3, Fig. 9a); core 4.1 has a close composition. CL-light rims 2.3 and 7.2 show 2–4 times decrease of REE, U, Th, Hf, Y, P, and Li. The rim 2.3 and altered core 3.1 contain small round heterogeneous inclusions, which in composition correspond to Mg-biotite (#mg = 0.67–0.70) with elevated Ti content (TiO_2 = 4–5 wt %). The same Ti–Bt forms intergrowth with quartz in the alteration zone in grain 10.

Measured $^{176}Hf/^{177}Hf_{(0)}$ ratios in zircon from metaorthopyroxenite UR82 plot in a range of 0.28033–0.28069. The lowest $^{176}Hf/^{177}Hf_{(0)} = 0.28033–0.28035$ (of all studied zircons from breccia rocks) and oldest model age values $t_{(Hf)}DM = 3.95$ Ga were obtained for zoned grain 6.1 and high-U grain 9.1. In Fig. 10c, they lie below the line $^{176}Lu/^{177}Hf = 0$ for protolith with $t(_{Hf})DM = 3.8$ Ga.

The high-U core of close age (point 7.1, concordant age of 3487 ± 4 Ma) differs in the elevated $^{176}Hf/^{177}Hf_{(0)} = 0.28060$. The same ratio of $^{176}Hf/^{177}Hf_{(0)} = 0.28059$ was obtained for core of grain 5.1. The elevated HREE and P contents and $^{176}Lu/^{177}Hf$ and $^{176}Yb/^{177}Hf$ isotope ratios in the grain 7.1 (Supplementary, Table EMS2) suggest the entrainment of Lu-rich zones or microinclusions in the measurement region.

Zircons with Pb^{207}/Pb^{206} age <3 Ga (grains 1.1, 3.1, 8.1) have the low $^{176}Hf/^{177}Hf_{(0)} = 0.28052–0.28055$ and $t_{(Hf)}DM = 3.7–3.6$ Ga. In Fig. 10c, they plot near the line $^{176}Lu/^{177}Hf = 0$ for protolith with $t(_{Hf})DM = 3.8$ Ga.

The high-U zircon 10.1 of the same age group has the elevated $^{176}Hf/^{177}Hf_{(0)} = 0.28069$. The $^{176}Hf/^{177}Hf_{(0)} = 0.28064$ close to that of 10.1 was determined also in the core of zircon 2.1, which gave the youngest Pb^{207}/Pb^{206} age values (~2 Ga).

Orthopyroxenite UR82/3. Zircon population is represented by oval or irregularly shaped grains, 200–400 μm in size (Fig. 8b). In CL, the grains show a composite inner structure, partly, with growth zoning (grain 2). Some oval grains (grain 4) retain relict of a zoned core rimmed by a young generation of CL-opaque zircon.

Isotope U-Pb age was measured and calculated for 10 domains from 9 grains (Table 2). All obtained age estimates have the great discordance from –6 to +19. The oldest age was obtained for a dark zoned core 8 with a Pb^{207}/Pb^{206} age of 3670 ± 5 Ma. It is enriched in REE (Table 3), the distribution pattern of which is similar to zircon spectra with an age of ~ 3.6 Ga from leucocratic enderbite UR82/1a.

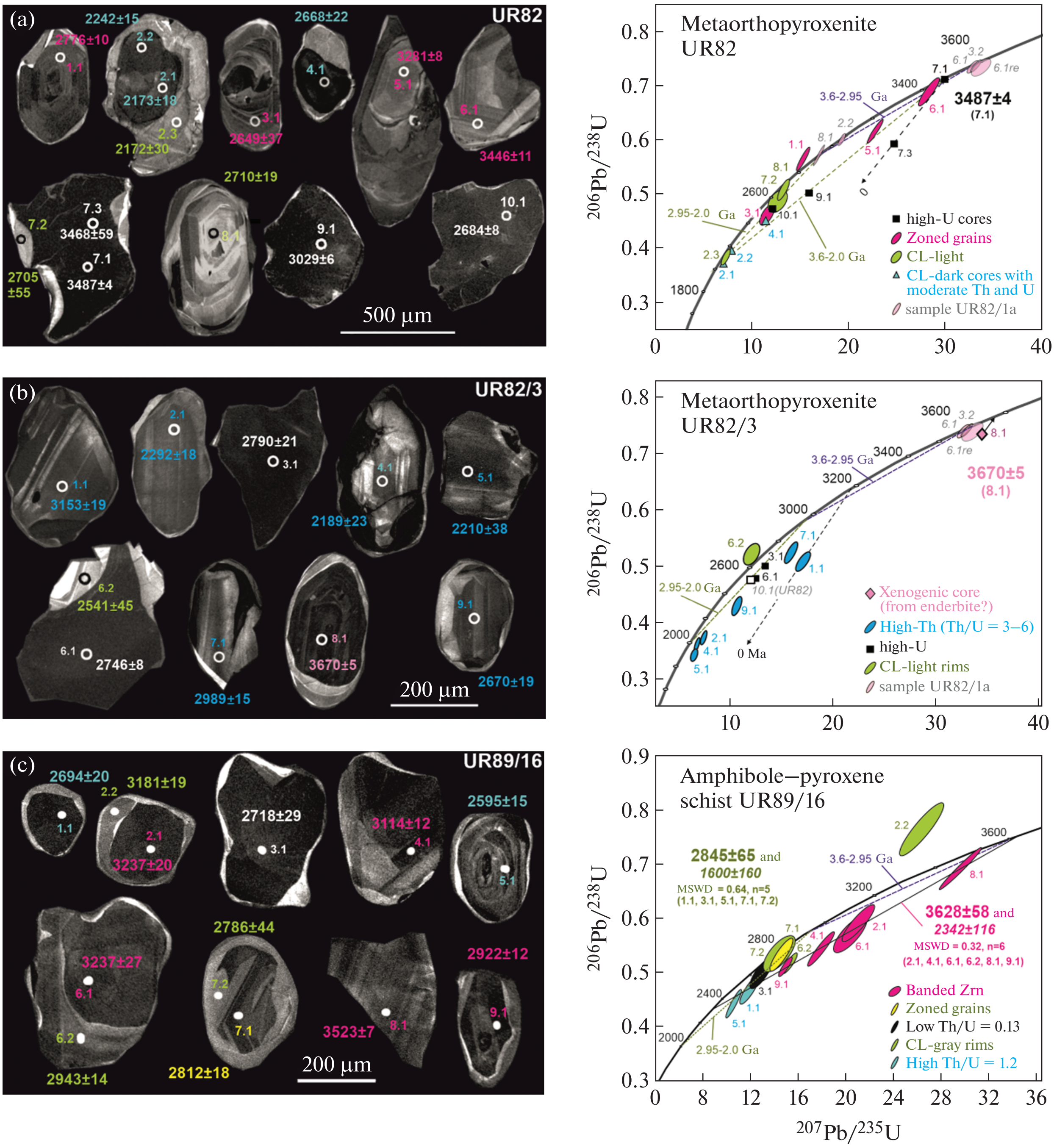

Fig. 8. Cathodoluminescence images of zircon and concordia diagrams. (a) for metaorthopyroxenite UR82, (b) metaorthopyroxenite UR82/3, (c) amphibole–pyroxene schists UR89/16. Point numbers in the U–Pb diagrams correspond to the point numbers in the cathodoluminescence images of zircon, where $^{207}Pb/^{206}Pb$ age is shown near the data point. Age is indicated in Ma. Subsidiary regression lines are shown: 3.6–2.0, 3.6–2.95, and 2.95–2.0 Ga.

Most part of the grains (1.1, 2.1, 4.1, 5.1, 7.1, 9.1) have an oval shape and stripped zoning typical of mafic rocks. They are surrounded by a heterogeneous zircon (Fig. 8b). Zircon of this group is sharply enriched in Th (250–1080 ppm) relative to U, and has Th/U = 3.4–5.9, Y (1443–1609 ppm), medium and heavy REE (725–785 ppm), P (282–418 ppm), and a distinct REE pattern (Fig. 9b). Point 1.1 gave the maximum $^{207}Pb/^{206}Pb$ age of 3159 ± 19 Ma, which defines the minimum age for this zircon type. The highest Th content (1080 ppm) was found in zircon 5.1, which contains inclusions of *Ap, Pl, Opx* (#mg = 0.6), *Cpx* (#mg = 0.79), and Ti-Bt (#mg = 0.63), as well as a *Kfs*–*Qz* intergrowth. Orthopyroxene inclusion (#mg = 0.66) surrounded by thin anthophyllite rim is shown in (Fig. 7e).

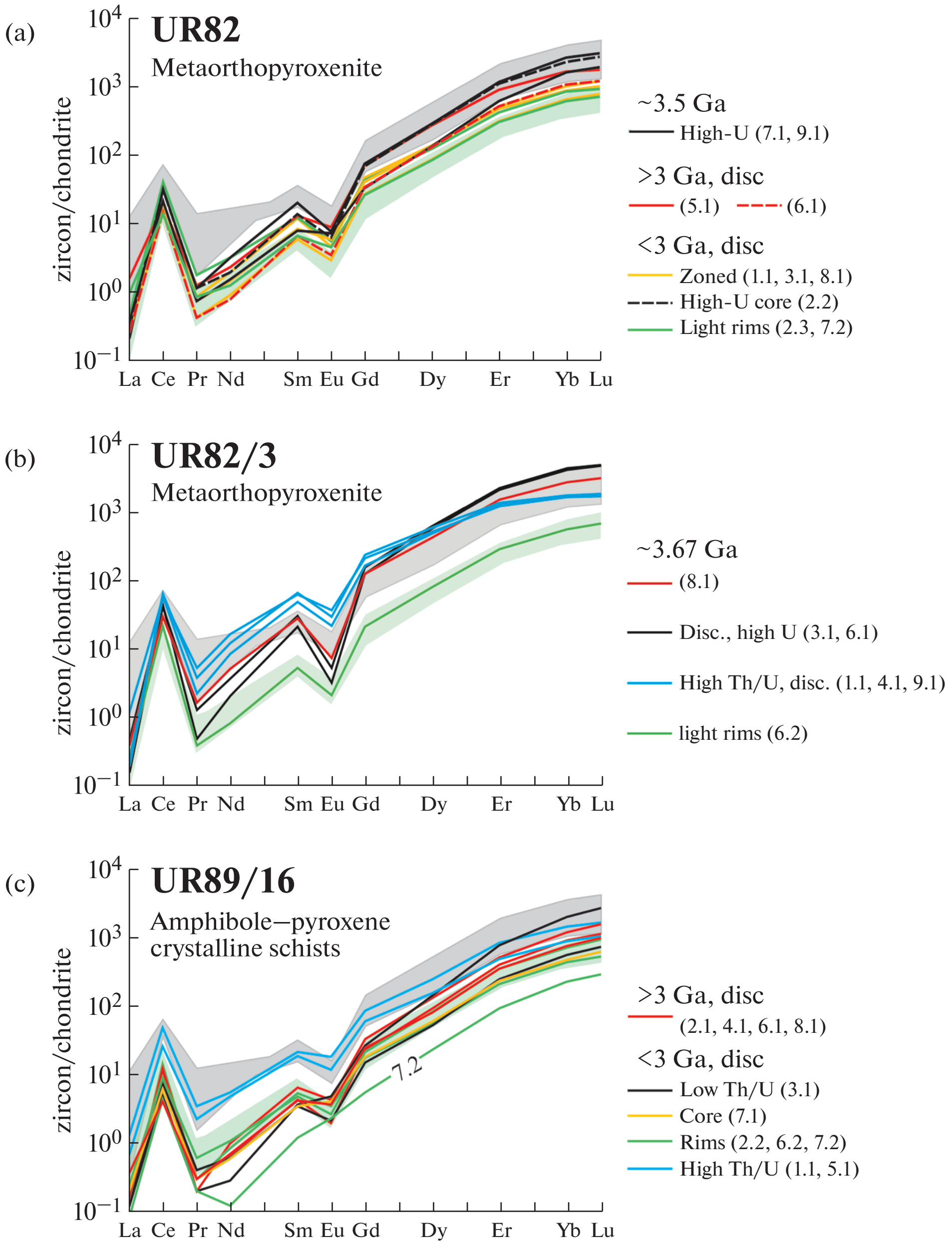

Fig. 9. Chondrite-normalized (Sun and McDonough, 1989) REE distribution pattern in zircon. (a) from metaorthopyroxenite UR82, (b) metaorthopyroxenite UR82/3, (c) amphibole–pyroxene schist UR89/16.

CL-opaque fragments (3.1 and 6.1) of high-U grains (U 518–1111 ppm) are characterized by the high contents of HREE (1400–1500 ppm), Y (2036–2130 ppm), P (589–826 ppm), and Li (14.6–25 ppm), and differ in the most differentiated REE distribution pattern ($(Lu/La)_n = 30$) (Table 3). In composition and morphology, they are similar to the high-U zircon grains from orthopyroxenite and fall on the concordia diagram near point 10.1 (UR82) on a 2.95–2.0 Ga regression line (Fig. 8b).

Amphibole-pyroxene schist (UR89/16). Zircon is represented by anhedral and oval, opaque, CL-gray and light gray grains (Fig. 8c). Some zircon fragments have a well-expressed zoning, and some grains consist of CL-dark cores with lighter rims (Fig. 8c). The grain size is 150–300 μm, CL-dark cores are slightly larger. Eight zircon grains (12 points) have been dated (Table 2). Most of obtained age estimates are discordant. The older zircon group (domains 2.1, 4.1, 6.1, 8.1, 9.1) with Pb^{207}/Pb^{206} ages of 2.9–3.5 Ga has a homogenous chemical composition, moderate U (177–294 ppm), Th (75–114 ppm), Th/U (0.3–0.64), and REE (Tables 2, 3; Fig. 9c) typical of magmatic zircons (Yakymchuk et al., 2018). In the U-Pb diagram, ana-

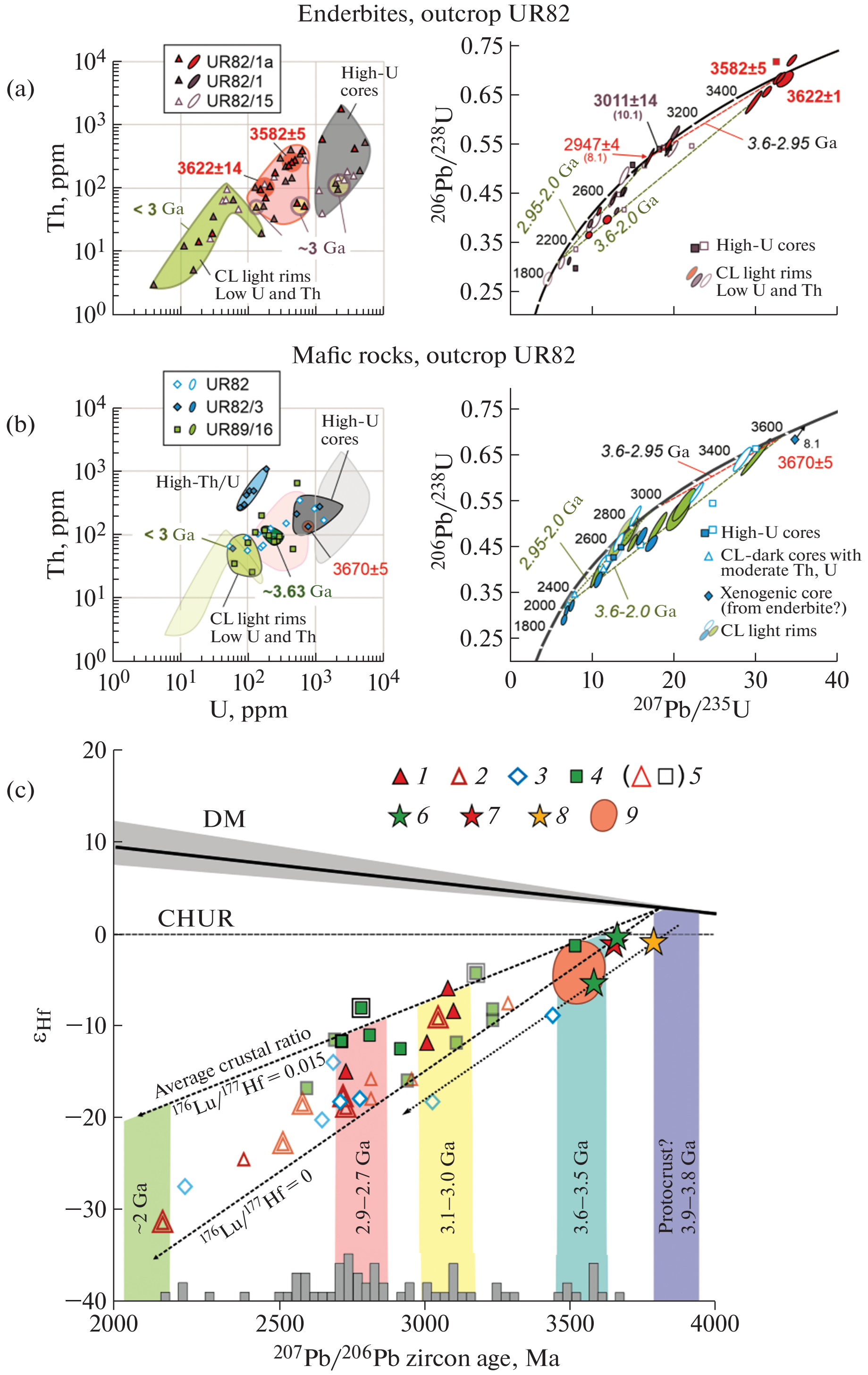

Fig. 10. Comparison of U and Th contents in zircon (on the left) and U–Pb isotope composition of zircon in the concordia diagram (on the right) for gneiss enderbite (a) and mafic inclusions (b) in the tectonomagmatic breccia of outcrop UR82; (c) diagram ε_{Hf}(t) – Pb^{207}/Pb^{206} age for the studied domains of zircon from rocks of tectonomagmatic breccia UR82 (*1*–*5*) compared to the composition of the oldest zircon grains of the Ukrainian shield (*6*–*9*). (*1*–*4*): zircon cores or central parts of the core-free zircon or central parts of core-free grains: (*1*) mesocratic enderbite UR82/1, (*2*) leucosome UR82/15, (*3*) metapyroxenite UR82, (*4*) amphibole–pyroxene schist UR89/16; (*5*) rims; bright symbols are zircon domains with discordance ≤5%, translucent with >5%. (*6*, *7*) Odessky quarry, Dniester–Bug province: (*6*) zircon from mafic granulite UR132 after (Lobach-Zhuchenko et al., 2013); (*7*) zircon from gneiss enderbite 06-BG-38 after (Bibikova et al., 2013); (*8*) zircon from quartzite of the Sorokinsky greenstone belt, Azov Province after (Claesson et al., 2015); (*9*) field of zircons with the oldest $^{207}Pb/^{206}Pb$ ages from gneiss enderbite 06-BG-38 (Odessky quarry) and 87-78 (Gaivaronsky quarry) (Shumlyanskyy et al., 2021). Localities of sample UR132 and 06-BG-38 are shown in Fig. 1c. The horizontal axis shows a relative histogram of Pb^{207}/Pb^{206} ages with discordance <10% for zircons from the rocks of the Odessky quarry, with peaks of tectonomagmatic activity in the studied region.

lytical data points plot beneath a 3.6–2.95 Ga regression line (Fig. 8c). Approximation of domains 2.1, 4.1, 6.1, 8.1, 9.1 by discordia yields an upper intercept age of 3628 ± 58 Ma (MSWD = 1.3) at lower intercept at around 2.3 Ga. The age value of 3628 ± 58 Ma within an error range corresponds to the previously obtained age of 3659 ± 19 Ma for one of zircon generations from granulite UR132 of the studied quarry (Lobach-Zhuchenko et al., 2017).

Zircon domains 1.1, 3.1, 5.1, 7.1, and 7.2 of different composition and structure (Tables 2, 3; Fig. 8c) lie near a 2.95–2.0 Ga regression line. The calculated discordia has an upper intercept age of 2845 ± 65 Ma at lower intercept of 1600 ± 160 Ma (MSWD = 0.64) (Fig. 8c). Zircons 1.1 and 5.1 at 3 times difference in U and Th contents have similar high Th/U = 1.2, REE contents and distribution patterns (Fig. 9c). Grain 3.1 is characterized by the extremely low Th/U = 0.13 and steep REE pattern: a sharp LREE depletion relative to HREE (Fig. 9c).

Zircon rims (2.2, 6.2, and 7.2) have the lowered contents of U (62–114 ppm), Th (25–72 ppm), and heavy REE (Tables 2, 3, Fig. 9c). Rims 2.2 and 6.2 have a Pb^{207}/Pb^{206} age around 2.9–3.1 Ga, which was recorded practically in all breccia rocks, although point 2.2 has a strong reverse discordance (–13).

The measured $^{176}Hf/^{177}Hf_{(0)}$ ratio varies from 0.28047 to 0.28079. Zircons with Pb^{207}/Pb^{206} age > 2.9 Ga (points 2.1, 4.1, 6.1, 8.1) are characterized by similar isotope composition and ratios of $^{176}Hf/^{177}Hf_{(0)}$ = 0.28047–0.28050. The same isotope ratios were obtained for undated zircon cores (points 13.2 and 16.1) and zircon rims (point 6.2). Values calculated for these seven points are as follows: $\varepsilon_{Hf}(3.63) = -0.5...+2$ and $t_{(Hf)}DM$ = 3.83–3.73 Ga (Fig. 10c). Some grains with a Pb^{207}/Pb^{206} age around 3 Ga (points 2.2, 9.1) and undated zircon cores 12, 14, 15 have higher ratios of $^{176}Hf/^{177}Hf_{(0)}$ = 0.28056–0.28063. Grains with Pb^{207}/Pb^{206} age < 2.85 Ga (points 1.1, 3.1, 5.1, 7.1, and 7.2) differ in the elevated isotope ratios: $^{176}Hf/^{177}Hf_{(0)}$ = 0.28067–0.28079 and in Fig. 10c plot above line $^{176}Lu/^{177}Hf = 0$ for protolith with $t(_{Hf})DM$ = 3.8 Ga. The same isotope ratios $^{176}Hf/^{177}Hf_{(0)}$ = 0.28069–0.28077 were obtained for undated rims of old zircon (points 13.1 and 16.2) and zircon (point 11) similar in morphology to zircon 1.1. Some parts of the grains (domains 3.1, 13.1, and 15) with elevated $^{176}Lu/^{177}Hf$ and $^{176}Yb/^{177}Hf$ ratios likely entrained microinclusions during measurement.

The zircons contain mineral inclusions *Opx* (#mg = 0.55–0.52), *Bt* (#mg = 0.62–0.65; TiO_2 = 4.8 wt.%), Qz (Fig. 7e), as well as separate inclusions and intergrowths of *Pl* (An_{47}–An_{39}), *Kfs*, *Bt* (#mg = 0.57, TiO_2 = 6.15 wt %) (Fig. 7g). *Opx* and *Bt* inclusions are located between old zircon core (13.2, $^{176}Hf/^{177}Hf_{(0)}$ = 0.28047) and rim (13.1, $^{176}Hf/^{177}Hf_{(0)}$ = 0.28069) (Fig. 7f).

PT-PARAMETERS OF THE FORMATION OF ROCK-FORMING MINERALS

The crystallization sequence of minerals was established from their relations observed in optical and scanning electron microscopes. Based on the mineral assemblage of the rock, we applied thermobarometric tools mentioned in section ANALYTICAL and in notes to table with results of *PT*-estimates (Table 4).

In the **mesocratic enderbite** (sample UR 82/1), the compositions of ortho- and clinopyroxenes define maximum temperatures within ~950–1030°C. However, in most cases, the compositions of these minerals reveal a temperature range of ~750–830°C based on different thermometers (Table 4). The pressure of mineral formation is estimated from amphibole, two-pyroxene, and hornblende–plagioclase barometers at 6–11 kbar (Table 4). Higher pressure values (around 11 kbar) were obtained on amphiboles formed after ilmenite. These amphiboles differ in the higher Mg#, the absence of Cr, and the high content of trivalent iron, which reflects the recrystallization under increasing fO_2.

Conditions of clinopyroxene formation in the mesoenderbite based on Al^{IV}–Al^{VI} relations correspond to the moderate- and low-pressure granulite facies (Fig. 4a). Clinopyroxene and orthopyroxene symplectites were formed at increasing temperature (Baba et al., 2018). An increase of temperature during formation of symplectites follows from an increase of Mg content in the clino- and orthopyroxene and anorthite molecule in plagioclase (Wells, 1977; Molina et al., 2015). A change of clinopyroxene composition expressed in an increase of Mg# with simultaneous increase of Fe^{3+} in mineral structure (from 0.01 to 0.07) reflects the transformation of the early assemblage with increasing fO_2 (Jan and Howie, 1981; Anderson and Smith, 1995).

Segregations of leucocratic minerals in the mesoenderbite rather represent the products of partial melting: plagioclase ($Ab_{58}An_{41}Or_1$) with myrmekites of *Kfs* (Ab_4Or_{96}) and quartz. Partial melting in leucocratic interlayers likely occurred simultaneously with symplectite crystallization. Inclusions of quartz and plagioclase (An_{41}) in zircon (z.4) that crystallized at 737°C likely belong to this type. Crystallization temperature of biotite in the mesocratic enderbite in compliance with the Ti and Mg# relations is around 700°C.

Based on the compositions of ortho- and clinopyroxene in **leucosome** (sample UR 82/15), the maximum equilibrium temperatures reached ~900–1080°C (Table 4). The mineral formation pressure based on the amphibole and two-pyroxene barometers is estimated at 5–11 kbar (Table 4). Maximum pressures based on the amphibole composition are estimated at 11 kbar. Late low-temperature hydrothermal processes are expressed in the replacement of clinopyroxene

Table 4. *PT*-estimate of the formation of rocks from a composite breccia

Sample no.	Description	*Amp-Pl* (M2015)	*Amp* (HZ86)	*Amp* (H87)	*Amp* (JR89)	*Amp* (S92)	*Amp* (M!6)	*OpxCpx* (P08)	Amp-Pl (HB1994)	*Cpx* (S08b 5/ 12 kbar)	*Opx* (M80a)	*OpxCpx* (P08 5/ 12 kbar)	*OpxCpx* (T98 5/ 12 kbar)	*OpxCpx* (WB73)	*OpxCpx* (W77)	*Ti-in-Bt* (WC15a)
		Pressure, kbar							Temperature, °C							
UR82	Coarse-grained metaortho-pyroxenite	4.8–6.0	5.2–6.3	5.5–6.7	4.2–5.1	5.6–6.6	5.1–5.3	2–6	643–704	653–657; 702–805; 731–836; 915	814–839; 856–983	719–865; 737–892	709–842	642–653; 761–805; 821–850; 876–892	721–768; 800–820; 872–884	550–630*
	Opx, *Bt* в *Zrn*	–	–	–	–	–		–	–	–	875	–	–	–	–	620–650*
UR82/1	Mesocratic enderbite	6.0–8.4; 8.6–10.0	7.1–7.7; 8.3–8.7; 9.4–11.4	7.6–12.4	5.8–9.4	7.5–11.5	6–11	5–15	632–639; 704–806	772–850; 816–899	949–1029	754–844; 775–870	722–809; 742–830	785–815	759–787; 993	660–665*
UR82/3	Medium-grained metaortho-pyroxenite	4.0–6.8	4.5–6.4	4.7–6.9	3.6–5.3	5.0–6.8	4–5.4	2.4–7.1	690–774	736; 776	969	774–802; 796–825	705–738; 724–757	809–834	788–816	635–670*
	Opx, *Cpx*, *Bt* in *Zrn*	–	–	–	–	–		–	–	995; 1140	815–910	825–905	928–955	910–915	940–950	670–715*
	Opx in *Zrn*, *Cpx* from matrix	–	–	–	–	–		–	–	–	–	735–810	705–750	810–830	805–825	–
UR82-15	Leucosome	–	6.4; 8.3	6.8; 8.9	5.2; 6.8	6.7; 8.5	4–7	4.7–7.2; 8.0–11.4	–	737–884; 778–934	860; 913–1078	771–930	703–841	772–841	774–879	620–660*
	Amp, *Bt* в *Zrn*	–	6.4	6.8	5.2	3.9; 6.8		–	–	–	–	–	–	–	–	710–750*
UR89-16	Amphi-bole—pyroxene schist	4.6–10.2	3.3; 6.7–7.1	3.4; 7.3–7.6	2.6; 5.3–5.8	3.9; 6.9–7.4	3; 5.5–6.1	2.0–12.0	711–776; 663–678	637–959; 681–1009	876–1024	748–912	625–888; 642–910	750–883	736–921	620–690*
	Bt in *Zrn*	–	–	–	–	–		–	–	–	–	–	–	–	–	670–710*

Pressure: *OpxCpx*(P08) – (Putirka 2008); *Amp-Pl* (M2015) – (Molina et al., 2015); *Amp* (HZ86) – (Hammarstrom, Zen, 1986); *Amp* (H87) – (Hollister et al., 1987); *Amp* (JR89) – (Johnson, Rutherford, 1989); *Amp* (S92) – (Schmidt, 1992), *Amp* (M16) – (Mutch et al., 2016). Temperature: *Amp-Pl*(HB1994) – (Holland, Blundy, 1994); *Cpx* (S08) – (Simakov, 2008); *Opx*(CM80a) – (Mercier, 1980); *OpxCpx* (P08) – (Putirka, 2008); *OpxCpx* (T98) – (Taylor, 1998); *OpxCpx* (WB73) – (Wood and Banno, 1973); *OpxCpx* (WS77) – (Wells, 1977); *Ti-in-Bt* (WC15a) – (Wu and Chen, 2015). * Calculations were made at 5 kbar.

inclusions in zircon by anthophyllite and grunerite at pressure of 4–5 kbar.

Crystallization temperature of phlogopite changes, with single exclusion, from 725°C to 675°C.

In the **metaorthopyroxenite** (sample UR82/3), recrystallization of orthopyroxene into a new *Opx,* assuming its somultaneous crystallization with late clinopyroxene, occurred at ~850°C according to equations (Witt-Eickschen and O`Neil, 2005). Most compositions of *Opx* and *Cpx* define temperatures of 730–830°C (Table 4).

Orthopyroxene inclusions in zircons differ in composition from matrix orthopyroxene. The latter together with clinopyroxene reveal crystallization temperature of ~730–830°C (Table 4), whereas *Opx* and *Cpx* inclusions in zircon give temperature of 930–950°C. This should indicate that matrix orthopyroxenes likely crystallized at post-peak conditions.

Phlogopite in the metaorthopyroxenite with decreasing Ti content in structure reflects a temperature decrease from ~700°C to 600–550°C.

According to Al^{IV}/Al^{VI} ratios (Fig. 4b), clinopyroxenes from metaorthopyroxenite UR82/3 correspond to diverse moderate and low pressures (Table 4). Sometimes, the observed predominance of trivalent iron in *Cpx* and unusually high (0.91) mg# likely reflect the later hydrothermal processes.

Hornblende from **metaorthopyroxenites** crystallized at a pressure of 4–7 kbar (Table 4). The latest actinolite–tremolite amphibole with #mg = 0.88–0.93 replaces pargasite and hornblende and was formed a pressure < 4 kbar.

In the **amphibole–pyroxene schist** (UR86/16), most clinopyroxenes in the diagram Al^{VI}/Al^{IV} (Figs. 4a, 4b) are plotted in the eclogite field. However, the low Na_2O concentrations and the absence of jadeite molecule do not allow us to ascribe clinopyroxene to the eclogite type. These pyroxenes likely experienced fluid-assisted reworking.

Based on the compositions of ortho- and clinopyroxene, the maximum temperatures of their joint crystallization are estimated at ~625–910°C, while the single-pyroxene orthopyroxene thermometer yields temperature up to 1024°C (Table 4).

The crystallization temperature of biotite, which is developed after amphibole, is ~650–725°C, which approximately corresponds to the lowest temperatures recorded by two-pyroxene thermometers (Table 4).

Pressure estimated from two-pyroxene barometer (Putirka, 2008) falls within a wide range, reaching up to 12 kbar (Table 4). Magnesian hornblende replacing pargasite has crystallized at lower (3–4 kbar) pressure. However, the pressure estimate could be affected by fO_2, an increase of which leads to the decrease of calculated pressure (Anderson and Smith, 1995). Pargasites from sample UR89/16 are characterized by the low $Fe^t/(Fe^t + Mg)$ values and in combination with low Al^t correspond to the high fO_2. Given these data, pargasite of the considered schist was likely recrystallized at pressure below 7 kbar.

DISCUSSION OF ISOTOPE DATA ON ZIRCONS AND RESULTS OF *PT*-ESTIMATES OF MINERAL FORMATION

Enderbites. The formation of the oldest U-Pb age value of 3622 ± 14 Ma (Fig. 5a) obtained for zircon from leucocratic enderbite UR82/1a could be related to the magmatic stage of rock evolution. Zircon with close ages of 3.6–3.75 Ga was established previously (Bibikova et al., 2013; Claesson et al., 2015, 2016; Shumlyanskyy et al., 2015; 2021) in the enderbites and metasedimentary rocks (quartzites and gneisses) of the Odessky, Zaval'evsky, Gaivarnosky, and Kazachii Yar quarries of the Dniester–Bug Province (Fig. 1a). This indicates that the enderbites from outcrop UR82 are ascribed to the earliest stage of crustal growth in this province.

Subsequent transformations of leucocratic enderbite UR82/1a recorded by the concordant zircon ages of 2947 ± 4, 3064 ± 6 Ma and 2090 ± 120, 2338 ± 89 Ma emphasize a complex evolution of the rocks. The position of some U-Pb data points of different zircon domains on the 3.6–2.95 and 3.6–2.0 Ga regression lines (Fig. 5a) reflects the different loss of radiogenic Pb by Eoarchean zircon during Mesoarchean and Paleoproterozoic metamorphic events, respectively.

Leucocratic enderbite UR82/1a represents the least altered fragment of primary magmatic (?) felsic rocks that preserve memory of their Paleoarchean age. The subsequent transformations of this rock are more clearly expressed in the mesocratic enderbite UR82/1 and leucosome UR82/15. U–Pb isotope system of zircon from these samples almost does not preserve memory of the Paleoarchean age and records metamorphic stages around 3.0, 2.8, and 2 Ga (Table 2, Figs. 5, 10). Most part of the U–Pb data points of different zircon domains of these samples lie below the concordia near the 2.95–2.0 Ga regression line (Fig. 10a) and reflect the different loss of radiogenic Pb by Mesoarchean zircon during Paleoproterozoic metamorphism. Thereby, the position of some zircon cores on the regression lines of 3.6–2.95 and 3.6–2.0 Ga (Fig. 10a) indicates the presence of primary Paleoarchean zircons in these samples. This conclusion is confirmed by the hafnium isotope composition of high-U zircon cores from leucosome UR82/15: they have the lowest isotope ratios of $^{176}Hf/^{177}Hf_{(0)}$ = 0.28046–0.28051, with calculated values of $t_{(Hf)}DM$ = 3.82–3.76 Ga. In Fig. 10c, their data points lie near the line $^{176}Lu/^{177}Hf = 0$ for protolith with $t_{(Hf)}DM$ = 3.8 Ga, which reflects the loss of radiogenic lead in metamorphic process. Close hafnium isotope composition was determined for the oldest zircons from enderbites of the Odessky and Gaivoronsky quarries (Fig. 10c).

The high-U zircon cores with concordant ages of 3–3.1 Ga for mesocratic enderbite UR82/1 differ in the elevated $^{176}Hf/^{177}Hf_{(0)}$ = 0.28055–0.28065. The same hafnium isotope composition is typical for marginal parts of old grains and light low-U rims with Pb^{207}/Pb^{206} age < 3.1 Ga for both mesocratic enderbite UR82/1 and leucosome UR82/15. In Fig. 10c, data points of these zircon domains lie between lines $^{176}Lu/^{177}Hf = 0$ and $^{176}Lu/^{177}Hf = 0.015$ for protolith with $t_{(Hf)}DM$ = 3.8 Ga. Such position of data points may indicate a partial isotope exchange between zircon and metamorphic fluid or recrystallization of zircon (especially rims) from metamorphic fluid.

Compared to zircon from leucoenderbite UR82/1a, zircon from mesocratic enderbite UR82/1 and leucosme UR82/15 in general is characterized by the low concentrations of REE (especially LREE), U, and Th; the lowest concentrations are observed in thin Paleoproterozoic rims (Fig. 10a). Such effect could be explained by the transformation of zircon during interaction with metamorphic fluid: zircon released Zr, Si, and trace components in fluid. Further fluid saturation in zirconium led to the crystallization of shells and new zircon domains in the dislocation zone. Newly formed zircon will be depleted in all incompatible components.

Most of mineral and melt inclusions only in high-U metamict cores of zircons from leucosome UR82/15 (Fig. 7b) indicate that these inclusions are related to the formation of anatectic melt of the leucosome under the granulite facies metamorphism. The latest transformations of the rocks were determined by the influence of H_2O-bearing fluid and led to the crystallization of amphibole and phlogopite. The altered zones of these zircon cores are characterized by the elevated REE (especially LREE) contents (Fig. 6c, grain 7.1). Thereby, the preserved fragments of the cores have low $^{176}Hf/^{177}Hf_{(0)}$ = 0.28046–0.28051, while their U–Pb data points (7.1, 8.1, 9.1) lie near the 3.6–2.0 Ga regression line (Fig. 5a), which indicates the Eoarchean age of primary zircon and its metamorphic transformation in the Paleoproterozoic.

The complex and multistage nature of rock formation suggests that the *PT*-parameters revealed for enderbites from mineral composition rather reflect the thermodynamic conditions of superimposed Proterozoic granulite metamorphism.

Mafic inclusions. Metaorthopyroxenites. Zircon from mafic inclusions also recorded a multistage evolution, where Paleoproterozoic (around 2 Ga) and Mesoarchean (around 2.8–3.0 Ga) stages are clearly distinguished (Fig. 10b). Thereby, some grains preserve memory of older processes. Some grains can be interpreted as entrapped from enderbites, for instance, core (8.1, sample UR82/3) with an Pb^{207}/Pb^{206} age of 3670 ± 5 Ma. It has the elevated U content typical of zircon from felsic rocks, and high crystallization temperature of 803°C (Table 3, Fig. 10b). The REE distribution pattern is similar to spectra of zircon with an age of ~3.6 Ga from gneiss enderbite UR82/1a (Fig. 9b). The composition of mineral inclusions in this zircon indicates its xenogenic origin supposedly from granitoid source. Discordant CL-opaque high-U zircon grains (3.1, 6.1, sample UR82/3) with high HREE contents have close crystallization temperature of 800–813°C (Table 3), and, likely, the same nature. They are similar to the high-U zircon grains from orthopyroxenite UR82 in composition and morphology and plot on the concordia diagram near point 10.1 (UR82) on a 2.95–2.0 Ga regression line (Fig. 8a).

Grains (6.1, 9.1, sample UR 8.2) with the lowest $^{176}Hf/^{177}Hf_{(0)}$ = 0.28033–0.28035 among all studied zircons from the breccia rocks can be also ascribed to xenogenic. In Fig. 10c, they plot below the line $^{176}Lu/^{177}Hf = 0$ for protolith with $t_{(Hf)}DM$ = 3.8 Ga; similar composition was determined for single zircons from mafic granulite UR132 and quartzites from the Sorokinsky greenstone belt of the Azov province (Fig. 10c). This indicates that the zircon was entrapped by orthopyroxenites from the older rocks than enderbites cementing breccia from outcrop UR82.

Other features of zircons from orthopyroxenites UR82 and UR82/3 are mainly different.

Most part of zircon grains from orthopyroxenite UR82/3 have morphology and zoning typical of mafic rocks and their primary crystallization was likely related to the magmatic stage of orthopyroxenite formation. However, these zircons show highly discordant U–Pb age values, extremely high Th/U ratio of 3.4–5.9 (Fig. 10b), and the low formation temperature of 690–750°C, calculated from Ti content (Table 3), which indicates a significant transformation of primary zircon. Estimated $^{207}Pb/^{206}Pb$ age and position of data points in the concordia diagram (Fig. 8b) suggest initially Meso–Paleoarchean age of orthopyroxenites with subsequent transformation in the Paleoproterozoic.

In metaorthopyroxenite UR82/3, pyroxene inclusions in zircons differ in composition from matrix pyroxenes. This is reflected in the temperature of their simultaneous crystallization: ~700–830°C in matrix and 930–950°C for pyroxene inclusions in zircon (Table 4). This fact indicates that the matrix pyroxenes could be recrystallized at the late metamorphic stage. A decrease of Al_2O_3 content (from 1.45 to 0.76 wt %) in orthopyroxene and anorthite content (from 44% to 38%) in plagioclase could be related to the influence of hydrous fluid (Morishita et al., 2003). Mesoarchean events are noted in all zircon grains from metaorthopyroxenite UR82, regardless of their structure and composition (Table 3, Fig. 8a).

All zircons from both studied samples obviously experienced significant transformations. Many zircon grains from metaorthopyroxenite UR82 are characterized by newly formed "lamellar" zones (Figs. 7c, 7d) enriched in FeO, Al_2O_3, MnO, CaO, and Na_2O, which is likely related to the low-temperature hydrothermal processes, as was shown in (Rayner et al., 2005). Such transformations, which sometimes spanned the entire central part of the grain, are also observed in other zircon grains from this sample (Fig. 7d). These domains frequently contain large inclusions: intergrowths of *Kfs*, *Pl* (An_{38-40}), *Opx*, and *Amp* in variable proportions. The absence of such forms of zircon alteration in other samples likely indicates that metaorthopyroxenite UR82 is confined to the local zone that was more permeable for metamorphic fluid and/or melt than other studied enclaves.

CL-zoned rims with low U, Th, and REE contents (Table 3, Fig. 10b) are typical of zircon from all studied samples of mafic enclaves; the contents of HREE, U, Th, Hf, Y, P, and Li in them show 2–4 times decrease compared to other zircon domains. As similar rims of enderbite zircon, they likely reflect the joint metamorphic transformation of the entire rock complex of tectonometamorphic breccia UR82 during Paleoproterozoic granulite metamorphism.

In general, a temperature change recorded from the compositions of orthopyroxenite minerals reflects a multistage mineral formation with a transition from the granulite facies to the low temperature amphibolite facies. It is noteworthy that the granulite facies also includes the higher temperature (930–950°C) and lower temperature (~800°C) stages (Table 4).

The oldest zircon group from **the amphibole—pyroxene schist UR89/16** with Pb^{207}/Pb^{206} ages of 2.9–3.5 Ga and geochemical characteristics typical of magmatic zircons (Yakymchuk et al., 2018), indicate the timing of magmatic crystallization around 3.6 Ga. These zircons are characterized by the low $^{176}Hf/^{177}Hf_{(0)}$ = 0.28047–0.28050 and old values of $t_{(Hf)}DM$ = 3.83–3.73 Ga, and their data points lie near the line of $^{176}Lu/^{177}Hf = 0$ for protolith with $t_{(Hf)}DM$ = 3.8 Ga (Fig. 10c). Close hafnium isotope age was obtained for zircon generation in mafic granulite UR132 from the studied quarry (Fig. 1c) with an age of 3659 ± 19 Ma (Lobach-Zhuchenko et al., 2017) (Fig. 10c). A scatter of analytical points along 3.6–2.95 Ga regression line (obtained on zircon from breccia matrix enderbite) could be related to the loss of radiogenic lead during Mesoarchean metamorphism, while the downward shift of data points could be related to the later loss of radiogenic Pb (Fig. 8c). The low temperature of zircon formation of 720–817°C calculated from Ti content (Table 3) likely corresponds to the Mesoarchean metamorphic stage, which is dated by core 9.1 and rim 6.2 at Pb^{207}/Pb^{206} age of 2.92–2.94 Ga. Rim (7.2) with younger Pb^{207}/Pb^{206} age around 2.8 Ga is characterized by the lowest REE, Y, Hf, P contents and crystallization temperature of 700°C compared to those of other domains. Mineral inclusions (*Opx*, *Bt*) are located between ancient zircon core (Fig. 7f) and rim, which was formed through the metamorphic recrystallization of zircon with entrapment of these minerals.

Grains with an Pb^{207}/Pb^{206} age < 2.85 Ga differ in the elevated $^{176}Hf/^{177}Hf_{(0)}$ = 0.28067–0.28079 and in Fig. 10c plot between lines $^{176}Lu/^{177}Hf = 0$ and $^{176}Lu/^{177}Hf = 0.015$ for protolith with $t_{(Hf)}DM$ = 3.8 Ga. Such position of data points can indicate a partial isotope exchange between zircon and metamorphic fluid or crystallization of zircon (shell) from fluid likely during Mesoarchean metamorphism. The Paleoproterozoic metamorphism led to the loss of radiogenic lead and a scatter of data points along an 2.9–2.0 Ga regression line (Figs. 8c, 10b).

In the amphibole–pyroxene schist, the *PT*-ranges of mineral formation coincide with the results for metaenderbites and metaorthopyroxenites (Table 4). This rock records the crystallization temperatures up to 1000–1020°C, which could be overestimated given their derivation from monomineral thermometers.

In the Dniester–Bug province, the oldest ages were obtained by U–Pb dating of terrigenous quartzites (around 3.8 Ga, Claesson et al., 2015). The Hf isotope geochemical characteristics of 3.75 Ga crust in the Azov and Podolsk provinces and 3.1 Ga crust in the Azov province characterize the Archean episodes in the polychronous evolution of new crust, as is considered in the work (Pietranik et al., 2008; Dhuime et al., 2012).

It is suggested (Shumlyanskyy et al., 2015; 2021) that the mafic and ultramafic rocks of the BGGD were formed through the high-degree melting of shallow garnet-free mantle containing Ti-bearing minerals and/or amphibole. It is believed that the enderbites were formed from a mixed eclogite source at depths and pressures corresponding to this source.

Presented data are consistent with a model of multistage evolution and polychronous growth of Archean crust, starting from the Paleo–Mesoarchean boundary. Based on the age and geochemical features of zircon (Claesson et al., 2015; Lobach-Zhuchenko et al., 2017; Claesson et al., 2019; Shumlyanskyy et al., 2021), the gneiss-enderbite complex, in addition to magmatic stages, records repeated structural-magmatic transformations, including an episode of the formation of tectonic breccia under the Archean granulite facies metamorphism. Including this stage, the gneiss enderbite complex represents diverse Archean episodes of the crustal growth from ~3.8 to 2.8–2.7 Ga. Archean rocks were subjected to the intense Paleoproterozoic transformations, which is typical of not only BGGD, but also of the entire Ukrainian and other shields around the world. In the studied rocks, Proterozoic processes caused partial and sometimes, complete reorganization of isotope and cation systems of minerals. It should be noted in this relation that zircon is a scarce mineral that preserved geochemical and isotope features sheding light on the rock evolution.

CONCLUSIONS

Obtained age and geochemical data on zircon together with *PT*-estimates of mineral formation reveal polychronous events from Archean to Proterozoic. Zircon contains inclusions of mineral phases, the compositions of which provide insight into thermodynamic conditions of the earlier mineral formation events, whereas the compositions of matrix minerals in different degree loss the primary geochemical features. However, some *PT*-estimates should be considered with caution, because mineral thermobarometric tools give no a direct indication to the attainment or preservation of chemical equilibrium between mineral phases. The U–Pb age estimates of different zircon domains and correlation of these ages with a change of Lu/Hf isotope ratios in this mineral are frequently ambiguous. But such situation is rather typical of rocks with long-term evolution spanning approximately 2 Ga.

In spite of the aforementioned difficulties, obtained results allowed us to distinguish the following stages of rock and mineral transformations:

(1) At 3.67–3.60 Ga, the earliest mineral assemblages were supposedly formed in enderbites, orthopyroxenites, and diverse orthoschists formed after mafic protolith at the magmatic stage.

(2) Mineral formation of the 3.0–2.8 Ga magmatic and metamorphic stage was responsible for the transformation of rocks with 3.67–3.60-Ga protozircon. At this stage, ~2.9 Ga, the products of partial melting of enderbites in form of such mineral phases as quartz, K-feldspar, and sodic plagioclase were entrained by Archean zircon.

(3) The U–Pb and Lu–Hf isotope systems of zircon and cationic systems of rock-forming minerals have been disturbed 2.0–1.9 Ga during Paleoproterozoic granulite metamorphism.

(4) Compositional evolution of rocks and minerals from tectonomagmatic breccia reflects episodes of polychronous growth of the Archean crust of the Ukrainian shield, starting from the Paleo- and Mesoarchean, with its structural and compositional rearrangement in the Paleoproterozoic.

SUPPLEMENTARY INFORMATION

The online version contains supplementary material available at https://doi.org/10.1134/S0016702925600026.

Table EMS1 is EDS compositions of minerals, Table EMS2-Lu-Hf isotope analyses of zircon.

ACKNOWLEDGMENTS

We, co-authors, are grateful to Svetlana Borisovna Lobach-Zhuchenko, the first author and initiator of this work, which unfortunately has been completed without her participation. We also thank Yu.A. Kostitsyn, the Scientific Editor, for organization and preparation of this manuscript. Kind comments and advices of T.V. Donskaya (Institute of the Earth's Crust, Siberian Branch, Russian Academy of Sciences) as well as anonymous reviewer allowed us to improve significantly the manuscript.

FUNDING

This work was supported by the Russian Ministry of Education for the Institute of Precambrian Geology and Geochronology, Russian Academy of Sciences (project no. FMUW-2022-0002).

CONFLICT OF INTEREST

The authors of this work declare that they have no conflicts of interest.

REFERENCES

J. L. Anderson and D. R. Smith, "The effects of temperature and f_{O2} on the Al-in-hornblende barometer," Am. Mineral **80** (5–6), 549–559 (1995).

C. R. Anhaeusser, "The anatomy of an extrusive-intrusive Archaean mafic-ultramafic sequence: The Nelshoogte schist belt and Stolzburg layered ultramafic complex, Barberton greenstone belt, South Africa," S. Afr. J. Geol. **104** (2), 167–204 (2001).

S. Baba, M. Uesato, T. Hokada, T. Adachi, Ya. Osanai, N. Nakano, and T. Toyoshima, "Metamorphic texture in mafic granulites collected from talus in the Brattnipene, Sor Rondane Mountains, East Antarctica," Bull. Faculty of Education. University of the Ryukyus **92** (2), 161–177 (2018).

J. Baldwin, S. Bowring, M. L. Williams, and I. Williams, "Eclogites of the Snowbird tectonic zone: petrological and U-Pb geochronological evidence for Paleoproterozoic high-pressure metamorphism in the western Canadian Shield," Contrib. Mineral. Petrol **147**, 528–548 (2004).

Sh. K. Baltybaev, S. B. Lobach-Zhuchenko, V. V. Balagansky, A. V. Yurchenko, Yu. S. Egorova, and E. S. Bogomolov, "Age and metamorphism of crystalline schists of the Pobuzh granulite complex of the Ukrainian Shield – ancient volcanics of the basement of the East European platform," Regional. Geol. Metallogen. **58**, 33–44 (2014).

E. V. Bibikova, S. Claesson, A. A. Fedotova, L. V. Stepanyuk, L. V. Shumlyanskyy, T. I. Kirnozova, M. M. Fugzan, and L. S. Il'insky, "Isotope–geochronological (U–Th–Pb, Lu–Hf) study of the zircons from the Archean magmatic and metasedimentary rocks of the Podolia Domain, Ukrainian Shield," Geochem. Int. **51** (2), 87–108 (2013).

L. P. Black, S. L. Kamo, and C. M. Allen, "Improved ^{206}Pb/^{238}U microprobe geochronology by the monitoring of a trace-element-related matrix effect: SHRIMP, ID-TIMS, ELA-ICP-MS and oxygen isotope documentation for a series of zircon standards," Chem. Geol **205**, 115–140 (2004).

T. D. Bocharnikova, V. V. Kholodnov, and E. S. Shagalov, "Mineral composition (apatite, magnetite, ilmenite, etc.) as a reflection of the processes of ore body formation and stratification in the Kusinsky gabbroic intrusion (Southern Urals).," Litosfera **19** (4), 533–557 (2019).

A. Bouvier, J. D. Vervoort, and P. J. Patchett, "The Lu–Hf and Sm–Nd isotopic composition of CHUR: constraints from unequilibrated chondrites and implications for the bulk composition of terrestrial planets," Earth Planet. Sci. Lett. **273**, 48–57 (2008).

V. V. Chashchin, T. B. Bayanova, E. E. Savchenko, D. V. Kiseleva, and P. A. Serov, "Petrogenesis and age of rocks from the Lower Zone of the Monchetundra mafic platinum-bearing massif, Kola Peninsula," Petrology **28** (2), 150–183 (2020).

S. Claesson, E. Bibikova, L. Shumanskyy, B. Dhuime, and C. J. Hawkesworth, "The oldest crust in the Ukrainian Shield – Eoarchaean U–Pb ages and Hf–Nd constraints from enderbites and metasediments," in *Continent Formation Through Time*, Ed. by N. M. W. Roberts, M. van Kranendonk, S. Parman, S. Shirey, and P. D. Clift (Geological Society, London, 2015), Vol. 389, pp. 227–259.

S. Claesson, G. Artemenko, S. Bogdanova, and L. Shumlyanskyy, "Archean crustal evolution in the Ukrainian Shield. Chapter 33," in *Earth's Oldest Rocks*, Ed. by M. J. Van Kranendonk, V. C. Bennett, and J. E. Hoffmann (Elsevier, 2019), pp. 837–854.

K. C. Condie, "Greenstones through times," in *Archean Crustal Evolution*, Ed. by K. C. Condie (Elsevier, 1994), pp. 85–120.

B. Dhuime, C. J. Hawkesworth, P. A. Cawood, and C. D. Storey, "A change in the geodynamics of continental growth 3 billion years ago," Science **335**, 1334–1336 (2012).

J. M. Ferry and E. B. Watson, "New thermodynamic models and revised calibrations for the Ti-inzircon and Zr-in-rutile thermometers," Contrib. Mineral. Petrol **154**, 429–437 (2007).

B. R. Frost, C. G. Barnes, W. J. Collins, R. J. Arculus, D. J. Ellis, and C. D. Frost, "A geochemical classification for granitic rocks," J. Petrol **42**, 2033–2048 (2001).

W. L. Griffin, N. J. Pearson, and E. Belousova, "The Hf isotope composition of cratonic mantle: LAM-MC-ICPMS analysis of zircon megacrysts in kimberlites," Geochim. Cosmochim. Acta **64**, 133–147 (2000).

W. L. Griffin, N. Nikolic, S. Y. O'reilly, and N. J. Pearson, "Coupling, decoupling and metasomatism: Evolution of crust–mantle relationships beneath NW Spitsbergen," Lithos **149**, 115–135 (2012).

J. M. Hammarstrom and E. Zen, "Aluminum in hornblende: an empirical igneous geobarometer," Am. Mineral **71**, 1297–1313 (1986).

S. L. Harley and L. P. Black, "A revised Archaean chronology for the Napier Complex, Enderby Land, from SHRIMP ion-microprobe studies," Antarct. Sci. **9** (1), 74–91 (1997).

R. P. Hartlaub, L. M. Heaman, A. Simonetti, and C. O. Böhm, "Relicts of Earth's earliest crust: U–Pb, Lu–Hf, and morphological characteristics of >3.7 Ga detrital zircon of the western Canadian Shield," in *Processes on the Early Earth*, Ed. by W. U. Reimold and R. L. Gibson, Geological Society of America Special Papers, Vol. 405 (2006), pp. 75–89.

D. J. Henry, J. Thomson, and C. V. Guidotti, "The Ti-saturation surface for low-to-medium pressure metapelitic biotites: Implications for geothermometry and Ti-substitution mechanisms," Am.Mineral **90** (2–3), 316–328 (2005).

T. Holland and J. Blundy, "Non-ideal interactions in calcic amphiboles and their bearing on amphibole–plagioclase thermometry," Contrib. Mineral. Petrol **116**, 433–447 (1994).

L. S. Hollister, G. C. Grisson, E. K. Peters, H. H. Stowell, and V. B. Sisson, "Confirmation of the empirical correlation of Al in hornblende with pressure of solidification of calc-alkaline plutons," Am. Mineral. **72**, 231–239 (1987).

H. Hui, Y. Niu, Zh, H. Zhao, D. Hei, and Zhu, "On the enigma of Nb–Ta and Zr–Hf fractionation—a critical review," J. Earth Sci. **22** (1), 52–66 (2011).

M. Q. Jan and R. A. Howie, "The mineralogy and geochemistry of the metamorphosed basic and ultrabasic rocks of the Jijal complex, Kohistan, NW Pakistan," J. Petrol **22**, 85–126 (1981).

M. C. Johnson and M. J. Rutherford, "Experimental calibration of an aluminum-in-hornblende geobarometer applicable to calc-alkaline rocks," Geology **17**, 837–841 (1989).

V. V. Kislyuk, V. V. Zyul'tsle, Z. M. Dorkovs'ka, L. V. Guk, V. V. Bondarenko, G. I. Chernets'ka, L. P. Nikitash, and G. V. Kislyuk, *National geological map of Ukraine. Scale 1 : 200000. Central Ukrainian Series. Arkush M-35—XXXVI* (Gaivoron) (Min-vo Ekol. Prir. Res. Ukr., 2011).

R. E. Leake, "Nomenclature of amphiboles," Can. Mineral **16**, 501–520 (1978).

S. B. Lobach-Zhuchenko, V. V. Balagansky, Sh. K. Baltybaev, L. M. Stepanyuk, A. N. Ponomarenko, K. I. Lokhov, M. Koreshkova, Yu, A. V. Yurchenko, Yu. S. Egorova, V. V. Sukach, N. A. Berezhnaya, and E. S. Bogomolov, "Formation stages of the Bug granulite complex: new structural-petrological and isotopic-geochronological data (Middle Bug region, Ukrainian Shield)," Mineral. Zh. **35** (4), 87–99 (2013).

S. B. Lobach-Zhuchenko, T. V. Kaulina, S. K. Baltybaev, V. V. Balagansky, Yu. S. Egorova, K. I. Lokhov, S. G. Skublov, V. V. Sukach, E. S. Bogomolov, L. M. Stepanyuk, O. L. Galankina, N. G. Berezhnaya, I. N. Kapitonov, A. V. Antonov, and S. A. Sergeev, "The long (3.7-2.1 Ga) and multistage evolution of the Bug Granulite-Gneiss Complex, Ukrainian Shield, based on the SIMS U-Pb ages and geochemistry of zircons from a single sample," in *Archaean Cratons - New Insights on Old Rocks*, Ed. by J. Halla, M. J. Whitehouse, T. Ahmad, and Z. Bagai (Geological Society London. Spec. Publications, 2017), Vol. 449, pp. 175–206.

C. B. Lobach-Zhuchenko, Yu. S. Egorova, Sh. K. Baltybaev, V. V. Balaganskii, L. M. Stepanyuk, A. V. Yurchenko, O. L. Galankina, E. S. Bogomolov, and V. V. Sukach, "Peridotites in the Paleoarchaean orthogneisses of the Bug granulite-gneiss area of the Ukrainian Shield: geologic position, compositional features, genesis," in *Evolution of the Material and Isotopic Composition of the Precambrian Lithosphere*, Ed. by Sh. K. Baltybaev and V. A. Glebovitsky (Izd.-Poligraf. Ass. Vyssh. Ucheb. Zaved., St. Petersburg, 2018), pp. 164–192.

S. B. Lobach-Zhuchenko, Sh. K. Baltybaev, Yu. S. Egorova, S. A. Sergeev, T. V. Kaulina, and T. E. Saltykova, "Stages of Paleoarchean to Paleoproterozoic basic–ultrabasic magmatism in the Sarmatian Craton," Russ. Geol. Geophys **63** (3), 267–290 (2022).

S. B. Lobach-Zhuchenko, Sh. K. Baltybaev, Yu. S. Egorova, and A. V. Yurchenko, "Archean phlogopite peridotite from gneissic enderbites of the Bug granulite-gneiss terrane (Ukrainian Shield): compositional features and possible mechanisms of its formation," Geochem. Int **61** (6), 593–629 (2023).

K. R. Ludwig, "SQUID 1.13a. A User's Manual. A Geochronological Toolkit for Microsoft Excel," Berkeley Geochronology Center Spec. Production **2**, 19 (2005).

K. R. Ludwig, "User's Manual for Isoplot Vers. 3.75. A geochronological toolkit for Microsoft Excel," Berkeley Geochronology Centre Spec. Publ. **5** (2012).

J. Mercier, "Single-pyroxene thermobarometry," Tectonophysics **70**, 1–37 (1980).

J. F. Molina, J. A. Moreno, A. Castro, C. Rodriguez, and G. B. Fershtater, "Calcic amphibole thermobarometry in metamorphic and igneous rocks: New calibrations based on plagioclase/amphibole Al-Si partitioning and amphibole/liquid Mg partitioning," Lithos **232**, 286–305 (2015).

T. Morishita, S. Arai, and D. H. Green, "Evolution of low-Al orthopyroxene in the Horoman Peridotite, Japan: an unusual indicator of metasomatising fluids," J. Petrol **44** (7), 1237–1246 (2003).

J.-F. Moyen and H. Martin, "Forty years of TTG research," Lithos **148**, 312–336 (2012).

E. J. F. Mutch, J. D. Blundy, B. C. Tattitch, F. J. Cooper, and R. A. Brooker, "An experimental study of amphibole stability in low-pressure granitic magmas and a revised Al-in-hornblende geobarometer," Contrib. Mineral. Petrol. **171** (2016). https://doi.org/10.1007/s00410-016-1298-9

G. S. Patrin, S. S. Matsyuk, S. I. Kostrovitskii, and N. V. Alymova, "Mineralogy and typochemistry of ilmenite from xenoliths of Upper Mantle rocks," Mineral. Zh. **26** (4), 60–77 (2004).

A. B. Pietranik, C. J. Hawkesworth, C. D. Storey, A. I. S. Kemp, K. N. Sircombe, M. J. Whitehouse, and W. Bleeker, "Episodic, mafic crust formation from 4.5 to 2.8 Ga: new evidence from detrital zircons, Slave craton," Can. Geol. **36**, 875–878 (2008).

K. Putirka, "Thermometers and Barometers for Volcanic Systems," in *Minerals, Inclusions and Volcanic Processes, Reviews in Mineralogy and Geochemistry*, Ed. by K. Putirka and F. Tepley (Mineral. Soc. Am., 2008), Vol. 69, pp. 61–120.

N. Rayner, R. A. Stern, and D. Carr, "Grain-scale variations in trace element composition of fluid-altered zircon, Acasta Gneiss Complex, northwestern Canada," Contrib. Mineral. Petrol. **148**, 721–734 (2005).

J. R. Reimink, J. H. F. L. Davies, T. Chacko, R. A. Stern, L. M. Heaman, C. Sarkar, U. Schaltegger, R. A. Creaser, and D. G. Pearson, "No evidence for hadean continental crust within Earth's oldest evolved rock unit," Nat. Geosci. **9** (10), 777–780 (2016).

F. J. M. Rietmeijer, "Chemical distinction between igneous and metamorphic orthopyroxenes especially those coexisting with Ca-rich clinopyroxenes: a re-evaluation," Mineral. Mag. **47** (343), 143–151 (1983).

E. Scherer, C. Carsten Münker, and K. Mezger, "Calibration of the Lutetium-Hafnium Clock," Science **293**, 683–687 (2001). https://doi.org/10.1126/science.106137

L. Schiotte, W. Compston, and D. Bridgewater, "Ion probe U–Th–Pb zircon dating of polymetamorphic orthogneisses from northern Labrador, Canada," Can. J. Earth Sci **26** (8), 1533–1556 (1989).

M. W. Schmidt, "Amphibole composition in tonalite as a function of pressure: an experimental calibration of the Al-in-hornblende barometer," Contrib. Mineral. Petrol **110** (2–3), 304–310 (1992).

L. Shumlyanskyy, C. Hawkesworth, B. Dhuime, K. Billström, S. Claesson, and C. Storey, "^{207}Pb/^{206}Pb ages and Hf isotope composition of zircons from sedimentary rocks of the Ukrainian shield: Crustal growth of the south-western part of East European craton from Archaean to Neoproterozoic," Precambrian Res. **260**, 39–54 (2015).

L. Shumlyanskyy, S. A. Wilde, A. A. Nemchin, S. Claesson, K. Billström, and B. Bagiński, "Eoarchean rock association in the Dniester-Bouh Domain of the Ukrainian Shield: A suite of LILE-depleted enderbites and mafic granulites," Precambrian Res. **352**, 106001 (2021).

S. K. Simakov, "Garnet-clinopyroxene and clinopyroxene geothermobarometry of deep mantle and crust eclogites and peridotites," Lithos **106**, 125–136 (2008).

J. S. Stacey and I. D. Kramers, "Approximation of terrestrial lead isotope evolution by a two-stage model," Earth and Planet Science Letters **26** (2), 207–221 (1975).

R. Stern and W. Bleeker, "Age of the world's oldest rocks refined using Canada's SHRIMP: The Acasta Gneiss Complex, Northwest Territories, Canada," Geoscience Canada **25** (1), 27–31 (1998).

S.-S. Sun and W. F. Mcdonough, "Chemical and isotopic systematics of oceanic basalts: implications for mantle composition and processes," Geol. Soc. London, Spec. Publ. **42** (1), 313–345 (1989).

S. A. Svetov, A. V. Stepanova, S. Yu Chazhengina, E. N. Svetova, Z. P. Rybnikova, A. I. Mikhailova, A. S. Paramonov, V. L. Utitsyna, M. V. Ekhova, and V. S. Kolodei, "Precision (ICP-MS, LA-ICP-MS) analysis of composition of rocks and minerals: technique and assessment of results by the example of the Early Precambrian mafic complexes," Tr. Karel'sk. Nauchn. Ts. RAN **7**, 54–73 (2015).

W. R. Taylor, "An experimental test of some geothermometer and geobarometer formulations for upper mantle peridotites with application to the thermobarometry of fertile lherzolite and garnet websterite," Neues Jahrb. Mineral., Abh. **172** (2-3), 381–408 (1998).

E. B. Watson, D. A. Wark, and J. B. Thomas, "Crystallization thermometers for zircon and rutile," Contrib. Miner. Petrol **151**, 413–433 (2006).

P. A. Wells, "Pyroxene thermometry in simple and complex systems," Contrib. Mineral. Petrol **62**, 129–139 (1977).

D. L. Whitney and B. W. Evans, "Abbreviations for names of rock-forming minerals," Am. Mineral. **95**, 185–187 (2010).

M. Wiedenbeck, P. Alle, and F. Corfu, "Three natural zircon standards for U–Th–Pb, Lu–Hf, trace element and REE analysis," Geostandard Newsletter **19**, 1–3 (1995).

I. S. Williams, *U-Th-Pb Geochronology by Ion Microprobe*, Ed. by M. A. McKibben, W. C. Shanks III, and W. I. Radley (Reviews in Economic Geology, 1998), Vol. 7.

G. Witt-Eickschen and H. S. C. O'Neill, "The effect of temperature on the equilibrium distribution of trace elements between clinopyroxene, orthopyroxene, olivine and spinel in upper mantle peridotite," Chem. Geol **221** (1–2), 65–101 (2005).

B. J. Wood and S. Banno, "Garnet–orthopyroxene and orthopyroxene–clinopyroxene relationships in simple and complex systems," Contrib. Mineral. Petrol **42** (2), 109–124 (1973).

C.-M. Wu and H.-X. Chen, "Revised Ti-in-biotite geothermometer for ilmenite- or rutile-bearing crustal metapelites," Sci. Bull. **60** (1), 116–121 (2015).

Ch. Yakymchuk, C. L. Kirkland, and C. Clark, "Th/U ratios in metamorphic zircon," J. Metamorph. Geol **36** (6), 715–737 (2018).

Translated by M. Bogina

SPELL: OK